Climate Dynamics (2006) 27: 493–513
DOI 10.1007/s00382-006-0144-6

Masakazu Yoshimori · Christoph C. Raible
Thomas F. Stocker · Manuel Renold

On the interpretation of low-latitude hydrological proxy records based on Maunder Minimum AOGCM simulations

Received: 19 August 2005 / Accepted: 24 March 2006 / Published online: 25 April 2006

Abstract An increasing number of proxy records, which are related to changes in the hydrological cycle, have been collected for climate reconstructions of the last millennium. There has been, however, little attempt to test climate models with such proxy records or to interpret proxy records using climate model simulations. In the present study, we analyze the hydrological changes between three different types of experiments: a present-day control, a perpetual AD 1640, and an ensemble of six transient Maunder Minimum (AD 1640–1715) simulations. Atmospheric moisture transport is investigated in terms of contributions of specific humidity and circulation changes. The study points out the importance of the specific humidity contribution to changes in moisture transport reflected in hydrological proxy records. The moisture budget of the western tropical Pacific is also investigated to aid the interpretation of a proxy record in this specific region. The present-day freshening of the western tropical Pacific, compared to the Maunder Minimum, is explained by the increased zonal moisture transport via trade winds, mainly due to the increased amount of atmospheric water vapor content in the warming world. Due to the existence of several uncertainty factors, such as forcing reconstructions, the link between the model simulations and proxy records is, however, not definitive, but the thermal contribution to hydrological proxy records is important and not limited to the Maunder Minimum period.

M. Yoshimori · C. C. Raible · T. F. Stocker · M. Renold
Climate and Environmental Physics, Physics Institute,
University of Bern, Bern, Switzerland

M. Yoshimori (✉)
Center for Environmental Prediction, Rutgers University,
14 College Farm Road, New Brunswick, NJ 08901-8551, USA
E-mail: masa@cep.rutgers.edu
Tel.: +1-732-9329735
Fax: +1-732-9328644

T. F. Stocker
International Pacific Research Center, SOEST,
University of Hawaii, Honolulu, HI, USA

1 Introduction

Large efforts have been made in reconstructing climate over the last millennium (Jones et al. 2001; Bradley et al. 2003; Jones and Mann 2004; Osborn and Briffa 2006). As the existence of instrumental records with a reasonably large geographical coverage is limited back to 150 years ago or so (Jones et al. 1999; Folland et al. 2001), reconstructions are based on proxy records for most of the millennium. Although some reconstructions of global or hemispheric mean temperature disagree with respect to the low-frequency component of the variability (Mann et al. 1999; Esper et al. 2002; von Storch et al. 2004; Moberg et al. 2005), they all support the detection of the recent climate change in that the late twentieth century warming is not consistent with the variability caused by natural factors alone (Bradley et al. 2003; Jones and Mann 2004; Osborn and Briffa 2006). While the principle and hence the validity of the formal detection and attribution of climate change are not constrained by details of the past climate evolution, they do rely on assumptions that the models simulate realistically internal variability and response to external forcing in both magnitude and spatial patterns (Mitchell et al. 2001). The climate of the last millennium is little affected by various anthropogenic factors for the most part, and hence provides a good opportunity to test such assumptions, if we know the forcing with a reasonable accuracy.

Unfortunately, there is a large uncertainty in the forcing history of the last millennium. Probably the most up-to-date uncertainty estimate in forcing between the Maunder Minimum (ca. AD 1645–1715, Eddy 1976) and present-day is given by Rind et al. (2004). They estimated the uncertainty of a factor of 8 in solar forcing and a factor of 2 in anthropogenic forcing. The reconstruction of volcanic forcing during the Maunder Minimum by Crowley (2000) is generally 2–3 times

larger than that of Robertson et al. (2001), and some significant volcanic events in one reconstruction are missing in the other (cf. Fig. 6 in Schmidt et al. 2004). Even for the relatively well-monitored 1991 Mount Pinatubo eruption, the radiative forcing estimated by Andronova et al. (1999) is about 1.5 times larger than that by Hansen et al. (2002).

In addition to thermal proxies, there is a growing number of proxy records which are related to changes in various components of the hydrological cycle (Jones and Mann 2004). However, climate model simulations have not yet been tested with such proxy records nor have they been used to interpret proxy records. It was demonstrated that, under weak external forcing such as that during the Maunder Minimum, the ratio between the externally forced signal and internally generated variability is small on regional scales, and it is often difficult to distinguish them (Yoshimori et al. 2005). Due to the chaotic component of internal variability, it is not realistic to anticipate that models reproduce the exact variability registered in proxy records. Therefore, in model-data comparison it is desirable to also make use of information of spatial variations (Shindell et al. 2001a). The spatial reconstructions are, however, still very rare (e.g., Mann et al. 1999; Luterbacher et al. 2002, 2004) due to the limitations of proxy records such as poor spatial coverage, limited temporal resolution, and dating uncertainty.

Due to the uncertainties in forcing and reconstructions, the consistent combination of forcing, mechanisms, and climate reconstructions currently represents a grand challenge. Nevertheless, an attempt to link the forcing and reconstruction, using a numerical model, is made here, rather than waiting for the emergence of definitive forcing data and the consensus on the climate reconstructions. The purpose of this paper is to present an overview of hydrological cycle changes in the Maunder Minimum simulations and to provide a general insight into the interpretation of hydrological proxy records. The presented results are obtained with a relatively-new coupled atmosphere–ocean general circulation model (AOGCM). However, it should be stressed that only one of many possible forcing scenarios is examined here.

Special attention is directed to the western tropical Pacific sea surface salinity changes which can be detected in coral records (Hendy et al. 2002). This serves as a more specific case study as it appears to represent relatively large-scale hydrological variability. Sea surface salinity in the western tropical Pacific exhibits persistent high values between the late sixteenth and mid-nineteenth centuries with a possible enhancement around the Maunder Minimum. This multi-century salinity anomaly approximately coincides with the so-called Little Ice Age (LIA), a prolonged cold period in the North Atlantic–European regions (Bradley and Jones 1993; Broecker 2000). Note that the global extent of the LIA is debated (Bradley et al. 2003; Jones and Mann 2004). The increased salinity is followed by a rather abrupt freshening, and low salinity continues till today. As briefly stated in Yoshimori et al. (2005), this is broadly consistent with our Maunder Minimum ensemble simulations conducted with an AOGCM. Hendy et al. (2002) hypothesized that stronger latitudinal temperature gradients during LIA intensified the Hadley circulation and increased the meridional moisture transport from the tropics to higher latitudes. They also speculated that LIA glacial expansion may have been driven by the increased poleward transport of water vapor from the tropical Pacific. A question arises as to the role of zonal moisture transport changes, because the magnitude of the moisture transport in the zonal direction is generally large near the tropics. Therefore, we evaluate the moisture budget of the region in the AOGCM simulations. Given the uncertainties in forcing alone, however, it is not possible nor our intention to disprove the original hypothesis. Rather, we raise a possibility of an alternative interpretation, which has a broad implication in understanding hydrological proxy records in general. Additionally, comparisons with other low-latitude hydrological proxy records are discussed which reveal the potential and limitation of the current model simulations.

The paper is organized as follows. Section 2 briefly presents the model description and experimental design. The analysis method is described in Sect. 3. The results are presented in Sect. 4, followed by the discussion and summary in Sects. 5 and 6, respectively.

2 Model and experiments

The model used and the experiments performed are same as those described by Yoshimori et al. (2005), to which the reader is referred for details. The model is the Community Climate System Model (CCSM) version 2.0.1 developed by the National Center for Atmospheric Research (NCAR) (Kiehl and Gent 2004). The model consists of atmosphere, ocean, land surface, and sea ice components, and they are coupled without flux corrections. The resolution of the model is approximately 3.75° in both longitude and latitude in the atmosphere with 26 vertical levels, and approximately 3.6° and 1.8° in the ocean with 25 vertical levels. Land and sea ice model components share the same horizontal resolutions with atmosphere and ocean, respectively. More detailed descriptions of the model are available at the NCAR CCSM web page (http://www.cgd.ucar.edu/csm/).

Three types of model simulations are conducted: present-day control (CTRL), steady Maunder Minimum (SMM), and transient Maunder Minimum (TMM) simulations. In the CTRL and SMM simulations, perpetual AD 1990 and 1640 forcings are applied, respectively (see Table 1 in Yoshimori et al. (2005) for actual forcing used). The equivalent radiative forcing in the SMM simulation relative to the CTRL simulation is about -2.5 Wm^{-2}. More than 85% of the difference is due to lower concentrations of well-mixed greenhouse gases (GHGs) and the rest is due to solar forcing. Other anthropogenic forcing agents are not included and constitute a large source of uncertainty, e.g., the indirect

Table 1 The annual moisture budgets of the CTRL simulation and of the difference between SMM and CTRL simulations in the western tropical Pacific

Variable	CTRL	SMM–CTRL
Precipitation (P)	2,304.2	−131.1
Evaporation (E)	1,813.5	−56.2
$P - E$	490.6	−74.8
F_W	−480.3	42.2
F_E	**−1,126.1**	**130.3**
F_S	−13.5	6.2
F_N	133.9	−6.0
$F_W - F_E$	645.8	−88.1
$F_S - F_N$	−147.5	12.2
$F_W - F_E + F_S - F_N$	498.3	−75.9

The unit is 10^6 kg s^{-1}. 100×10^6 kg s^{-1} corresponds to approximately 0.25 mm day^{-1} in this region with the area of $\sim 33.9 \times 10^6$ km^2. The dominant term in the lateral moisture fluxes is highlighted in bold. See Fig. 2 for the definition of the variables

effect of aerosols (Rind et al. 2004). The detailed discussion on the forcing uncertainty and its implication for the results are given in Sect. 5. For the TMM simulations, a time-varying forcing from AD 1640 to 1715, which includes the effect of solar activity and major volcanic eruptions, is imposed (Fig. 1). The volcanic forcing data are adopted from Crowley (2000). The solar forcing data are constructed based on Crowley (2000) and Lean et al. (1992, 1995). Solar forcing time series by Crowley (2000) is adjusted so that it yields approximately 0.24% reduction in total solar irradiance (TSI) during the Maunder Minimum relative to the present-day, as suggested by Lean et al. (1992, 1995). The magnitude of the reduction is rather arbitrary as the current estimate in solar forcing reduction during the Maunder Minimum ranges from about 0.05 to 0.4%, although recent estimates tend to favor smaller reductions (Rind et al. 2004). Note that relatively similar values are used in other studies: e.g., nearly identical values in Zorita et al. (2004), reductions of 0.25% in Rind and Overpeck (1993) and Rind et al. (1999), 0.35% in Cubasch et al. (1997), and 0.2% in Rind et al. (2004). The forcing is crudely represented in terms of changes in TSI with an equal fractional change over the spectrum. Representing the effect of volcanic aerosols as a reduction of solar irradiance introduces some uncertainties in high-latitude regional winter responses by not accurately capturing the positive annular mode invoked by warming in the low-latitude lower stratosphere in the winters following eruptions (Shindell et al. 2001a), while the model does simulate the correct sign of annular mode with a weak magnitude for different reasons (Yoshimori et al. 2005). The solar forcing gradually decreases from 1640 to 1688 by 1.30 Wm^{-2} in TSI, followed by a continuous increase until 1715 by 0.47 Wm^{-2}. There are five major volcanic events: AD 1641, 1667, 1674, 1681, and 1695. These volcanic forcing peaks range from −22.0 to −9.6 Wm^{-2} in TSI. GHG concentrations are fixed at the level in AD 1640. Consequently, the TMM simulation in any given year has a negative radiative forcing relative to the SMM simulation. Six TMM ensemble members are produced with slightly different initial conditions but identical boundary conditions.

3 Analysis method

We use conventional three-month seasons for the seasonal averages, i.e., December–January–February (DJF), March–April–May (MAM), June–July–August (JJA), and September–October–November (SON). Three-dimensional data are first vertically interpolated from hybrid sigma-pressure model coordinates to the 17 pressure levels used in the NCEP-NCAR re-analysis dataset before conducting the analyses, unless noted otherwise.

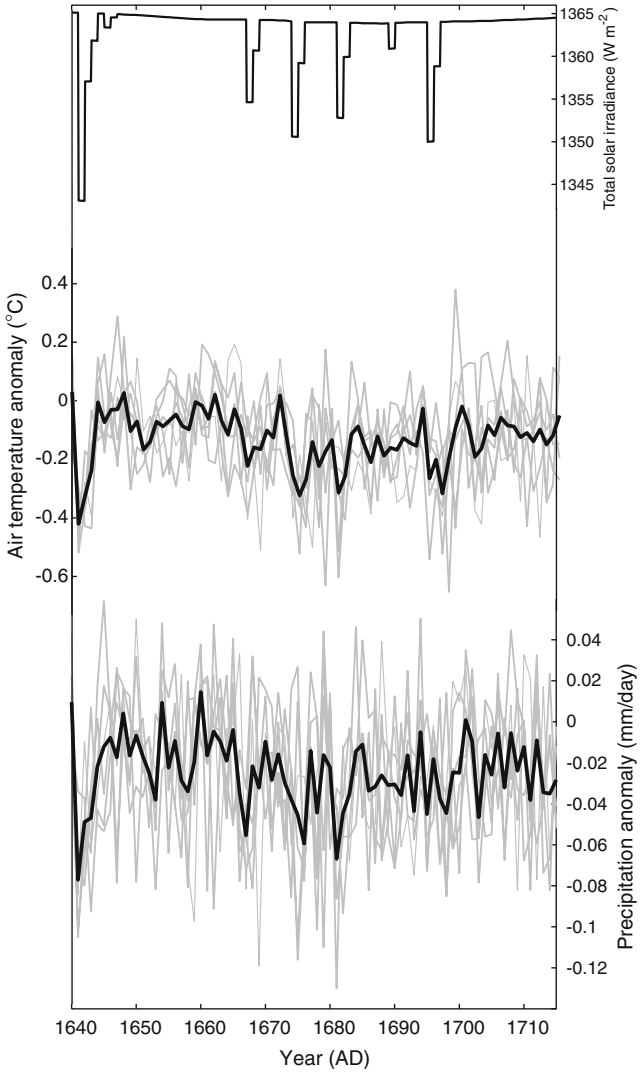

Fig. 1 *Top* Solar irradiance imposed in the TMM simulations representing gradual solar activity changes and volcanic eruptions. *Middle* Simulated, annual mean tropical surface air temperature anomaly between 20°S and 20°N. Here the anomaly is referred to as the TMM simulations relative to the mean of the SMM simulation. *Bottom* Same as in the middle, but for precipitation rate anomaly. *Gray lines* represent each ensemble member in the TMM simulations, and *thick solid line* represents the TMM ensemble mean

The moisture transport is calculated from the daily output of the model. The change in hydrological cycle is investigated with three main measures: meridional distribution of moisture, horizontal moisture transport, and moisture budget of a specific region.

First, the zonal mean analysis is conducted to obtain an overview of the hydrological response of the model to external forcing. The meridional moisture transport is investigated. The difference in the meridional moisture transport between two experiments (e.g., SMM vs. CTRL) is decomposed into the time-mean and transient eddy components:

$$\Delta[\overline{v}\overline{q}] = \Delta[\overline{v}][\overline{q}] + \Delta\left[\overline{v'q'}\right], \tag{1}$$

where v and q are meridional velocity and specific humidity, respectively, and Δ denotes the difference between the two experiments. The bar and square bracket denote seasonal and zonal means, respectively, and the prime denotes deviations from the seasonal mean. The time-mean component is further decomposed into four contributions:

$$\Delta[\overline{v}\overline{q}] = [\overline{v}]\Delta[\overline{q}] + [\overline{q}]\Delta[\overline{v}] + \Delta[\overline{v}]\Delta[\overline{q}] + \Delta[\overline{v}^*\overline{q}^*]. \tag{2}$$

The first term on the right hand side represents the change in meridional moisture transport due to the change in zonal mean specific humidity alone, while the second term represents the contribution of the meridional circulation change alone. The third term represents the covariance between the specific humidity and meridional circulation, and the last term represents the stationary eddy contribution. The covariance term may be interpreted as the amplified moisture transport due to the fact that both specific humidity and meridional circulation may vary. This does not mean, however, that there is a causal relationship between the two. The decomposed seasonal terms are vertically-integrated and averaged to obtain annual mean column-integrated moisture transport. This decomposition method allows us to address to what extent the change in zonal mean meridional circulation, or the Hadley circulation, accounts for the change in the meridional moisture transport. In other words, it reveals the extent to which the strength of the Hadley circulation can be inferred solely from hydrological proxy records.

Second, the horizontal moisture transport is calculated to investigate the zonally asymmetric part of the hydrological response to external forcing. As in the zonal mean analysis, the difference in the horizontal moisture transport between two experiments is decomposed into the time-mean and transient eddy components:

$$\Delta(\overline{u}\overline{q}, \overline{v}\overline{q}) = \Delta(\overline{u}\overline{q}, \overline{v}\overline{q}) + \Delta\left(\overline{u'q'}, \overline{v'q'}\right), \tag{3}$$

where u is zonal velocity. The time-mean component is further decomposed into three contributions:

$$\Delta(\overline{u}\overline{q}, \overline{v}\overline{q}) = (\overline{u}, \overline{v})\Delta\overline{q} + \overline{q}\Delta(\overline{u}, \overline{v}) + (\Delta\overline{u}\Delta\overline{q}, \Delta\overline{v}\Delta\overline{q}). \tag{4}$$

The first and second terms on the right hand side represent the contributions of changes in local specific humidity and wind velocity, respectively, and the third term is the covariance of the two. Note that the same decomposition method was employed in Clement et al. (2004).

Third, the moisture budget of a specific region is investigated. At the boundaries of the region, vertically-integrated zonal and meridional moisture fluxes are calculated as follows (Fig. 2):

$$\begin{aligned} F_{\mathrm{W,E}} &= -\frac{a}{g}\int_{\phi_S}^{\phi_\mathrm{N}}\int_{p_\mathrm{s}}^{p_\mathrm{t}} u(\lambda = \lambda_{\mathrm{W,E}}, \phi, p) \\ &\quad \times q(\lambda = \lambda_{\mathrm{W,E}}, \phi, p)\cdot \mathrm{d}p \cdot \mathrm{d}\phi, \\ F_{\mathrm{S,N}} &= -\frac{a\cos\phi}{g}\int_{\lambda_\mathrm{W}}^{\lambda_\mathrm{E}}\int_{p_\mathrm{s}}^{p_\mathrm{t}} v(\lambda, \phi = \phi_{\mathrm{S,N}}, p) \\ &\quad \times q(\lambda, \phi = \phi_{\mathrm{S,N}}, p)\cdot \mathrm{d}p \cdot \mathrm{d}\lambda, \end{aligned} \tag{5}$$

where p_s and p_t denote the pressure at the surface and the top of atmosphere, respectively. λ, ϕ, and p are longitude, latitude, and pressure, respectively, and a and g are the radius of the Earth and gravitational acceleration, respectively. Here the vertical integration is calculated on the model coordinates without interpolation.

4 Results

In the following, most results are presented as the difference between the SMM and CTRL simulations (SMM–CTRL), and the difference between the TMM and SMM simulations (TMM–SMM). All presented results are 75-year averages whose length is determined by each TMM simulation unless noted otherwise. Multi-decadal averages are taken to maximize the signal-to-noise ratio, and to explore the gross features of the Maunder Minimum. This does not mean that model

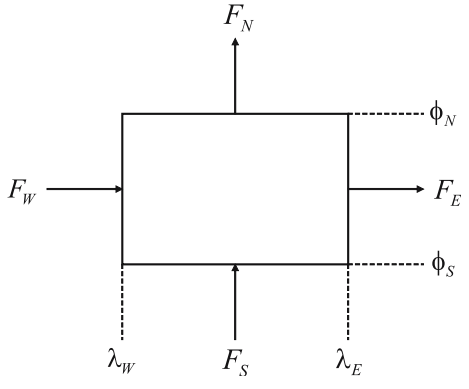

Fig. 2 Definition of horizontal moisture fluxes at boundaries of a specific region of interest. λ_W and λ_E denote longitudes at the western and eastern boundaries, respectively, while ϕ_S and ϕ_N denote latitudes at the southern and northern boundaries, respectively. Similarly, F_W and F_E are the vertically-integrated eastward moisture fluxes at the western and eastern boundaries, respectively, while F_S and F_N denote vertically-integrated northward moisture fluxes at the southern and northern boundaries, respectively

responses are similar if a time-mean forcing is applied instead of a time-varying forcing. To exhibit the flavor of the transient ensemble simulations, tropical temperature and precipitation time series are shown in Fig. 1. SMM–CTRL mainly represents the response to anthropogenic GHGs or qualitatively the difference between the long-term pre-industrial mean and present-day climate. On the other hand, TMM–SMM represents the response to the external forcing unique to the Maunder Minimum. Therefore, the difference between the Maunder Minimum and present-day climate is given as a sum of the two, i.e., (TMM–CTRL) = (TMM–SMM) + (SMM–CTRL). In most cases, TMM–SMM is an order of magnitude smaller than SMM–CTRL.

4.1 Meridional distribution of moisture

Zonal mean near-surface air temperature and difference between precipitation and evaporation ($P - E$) are shown in Fig. 3. Zonal mean temperature in SMM–CTRL exhibits globally colder temperatures with enhanced coolings in Polar regions (1.50°C cooling on global average, Fig. 3a). This increased meridional temperature gradient with a stronger response in the Northern Hemisphere is a well known feature of climate change forced by well-mixed GHGs. The high latitude cooling is larger over the ocean due to increased surface albedo and decreased heat exchange between the atmosphere and ocean, associated with the

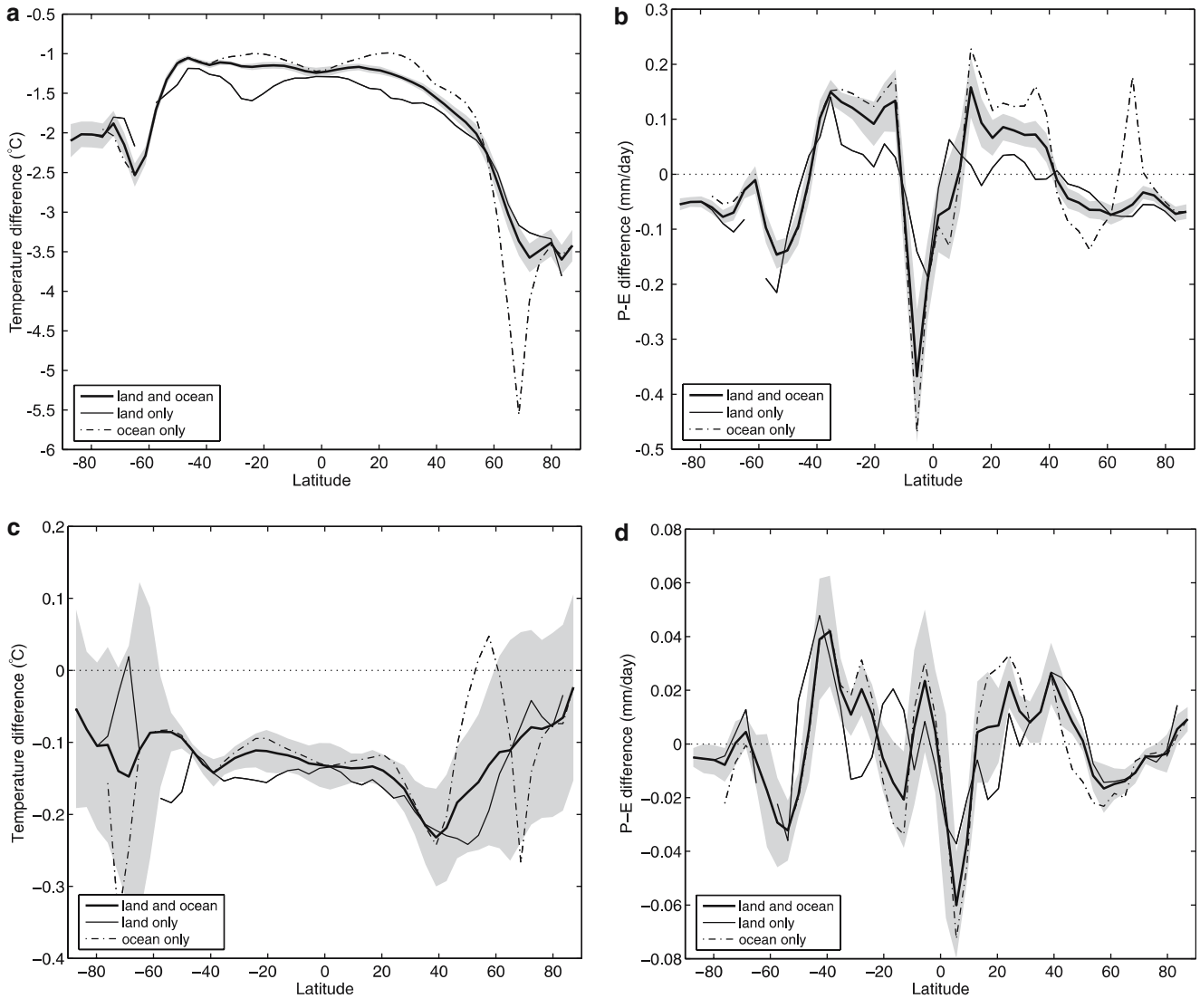

Fig. 3 Annual and zonal mean fields: **a** near-surface air temperature difference between the SMM and CTRL simulations; **b** $P - E$ (precipitation minus evaporation) difference between the SMM and CTRL simulations; **c** near-surface air temperature difference between the TMM ensemble mean and the SMM simulation; and **d** $P - E$ difference between the TMM ensemble mean and the SMM simulation. *Thick solid*, *thin solid*, and *thin dash-dotted lines* represent the zonal mean values over both land and ocean, only over land, and only over ocean, respectively. *Shading* in **a** and **b** represent 95% confidence intervals for the estimate of the population differences calculated with the Welch approximation (Devore 1987). *Shading* in **c** and **d** represent ± 1 standard deviation of the TMM ensemble members centered on its mean. *All shadings* correspond to "land and ocean"

change in sea ice cover. In low latitudes, cooling over the ocean is more pronounced near the equator than in the subtropics (~20°), reducing the temperature gradient there. This response is consistent with changes in the net shortwave radiation at the top of the atmosphere and greenhouse efficiency: a decrease near the equator and a slight increase in the subtropics. The change in the net shortwave radiation is accompanied by an increase in low-level cloud cover near the equator (absolute change of +0.4%) and a decrease in the subtropics (−1.7%). On the other hand, the change in greenhouse efficiency is accompanied by a decrease in high-level cloud cover near the equator (−0.5%) and an increase in the subtropics (+1.0%). In addition to the cloud feedback, water vapor feedback likely contributes to the larger cooling near the equator than in the subtropics. Zonal mean $P - E$ in SMM–CTRL shows a decrease in the tropics (~5°S) and high latitudes (~40°–90°) and an increase in the subtropics (~10°–40°) (Fig. 3b). This implies a reduced meridional moisture transport from the subtropics to the tropics and to high latitudes. The $P - E$ change is more pronounced over the ocean than over land, as expected from the fact that the hydrological cycle is more active over the ocean in the present-day climate. In addition, the reduction of $P - E$ over land is limited by the availability of soil moisture. Note that the large increase in $P - E$ in northern high latitudes over the ocean (~70°N) reflects a reduction of evaporation associated with the change in sea ice cover.

Zonal mean temperature in TMM–SMM exhibits consistent low-latitude cooling in all ensemble members but a large ensemble spread in the high latitudes (0.13°C cooling on global average, Fig. 3c). Although all ensemble members tend to show cooling in high latitudes, the sign of meridional temperature gradient changes is not clear, particularly in the Southern Hemisphere. This may reflect the effect of volcanic forcing which typically cools low latitudes more effectively than high latitudes as shown in both observational records and model simulations (Robock and Liu 1994; Robock and Mao 1995). In addition, high latitudes are characterized by large internal variability which could result in the spread of the ensemble under the weak forcing. For the same reason as for SMM–CTRL, the cooling near the equator is slightly larger than in the subtropics (~20°) over the ocean. Contrary to the temperature, zonal mean $P - E$ exhibits a small ensemble spread (Fig. 3d). At a first glance, this appears to contradict the regional analysis over land in Yoshimori et al. (2005) in which temperature generally shows a much better signal-to-noise ratio than precipitation. This is because the ensemble spread in temperature is pronounced mainly over the ocean. The zonal mean $P - E$ shows a decrease in the tropics (~5°N) and high latitudes (~50–90°), and an increase in the subtropics and mid latitudes (~20–50°). Again, this implies a reduced meridional moisture transport from the subtropics and mid-latitude to the tropics and to high latitudes although the magnitude is much smaller than SMM–CTRL due to the weaker forcing.

Precipitation and evaporation changes are mainly determined by precipitation changes in the tropics and by evaporation changes in the subtropics (Fig. 4a, c). Evaporation shows relatively uniform reductions while precipitation changes exhibit a distinct meridional structure. The reduced evaporation in the subtropics does not result in the reduction of precipitation there, but in the tropics. Also, the sign of the precipitation change in the subtropics is marginally positive in spite of the evaporation decreases there. The difference in $P - E$ in SMM–CTRL exhibits little seasonal variations whereas TMM–SMM varies with seasons (Fig. 4b, d). This contrast in pattern suggests that the dominant mechanism associated with the $P - E$ change in SMM–CTRL may be different from TMM–SMM, and that the dominant mechanism for SMM–CTRL works in all seasons.

As described in Sect. 3, the meridional moisture transport is investigated by decomposing it first into a time-mean and a transient eddy component. As expected, the time-mean component dominates over the transient eddy component in the moisture transport in low latitudes (~20°S–20°N, Fig. 5a, c). On the contrary, the two components are comparable in mid latitudes. The transient eddy component exhibits different response patterns between SMM–CTRL and TMM–SMM, in addition to the magnitude. In the former, the poleward transient eddy moisture transport decreases in both hemispheres while it increases in the latter. In both cases, eddy activity, indicated by eddy kinetic energy, increases in lower and mid troposphere throughout the year (not shown). In SMM–CTRL, however, a strong cooling in low latitudes results in a larger reduction of the meridional gradient of atmospheric water vapor content, which leads to the net reduction of moisture transport even with the enhanced eddy mixing.

A further decomposition of the time-mean component in SMM–CTRL reveals the dominance of the effect of the specific humidity change in the tropics (Fig. 5b). Near the equator, however, there is a non-negligible effect of the circulation change. Colder temperature in the SMM simulation leads to a lowered saturation specific humidity according to the Clausius–Clapeyron relation while the relative humidity stays at similar levels, resulting in a reduced specific humidity (cf. Genfo et al. 1991; Held and Soden 2000; Wentz and Schabel 2000). Since the meridional circulation transports moisture from the subtropics to the tropics, the reduction of specific humidity or atmospheric water vapor content results in a reduction of meridional moisture transport. The dominance of the effect of the specific humidity change over the circulation change is consistent with the fact that changes in $P - E$ occur similarly in all seasons as depicted in Fig. 4b. It may be worth noting that the stationary eddy contribution is dominant in the time-mean component in the Northern Hemisphere mid latitudes, suggesting that the interpretation

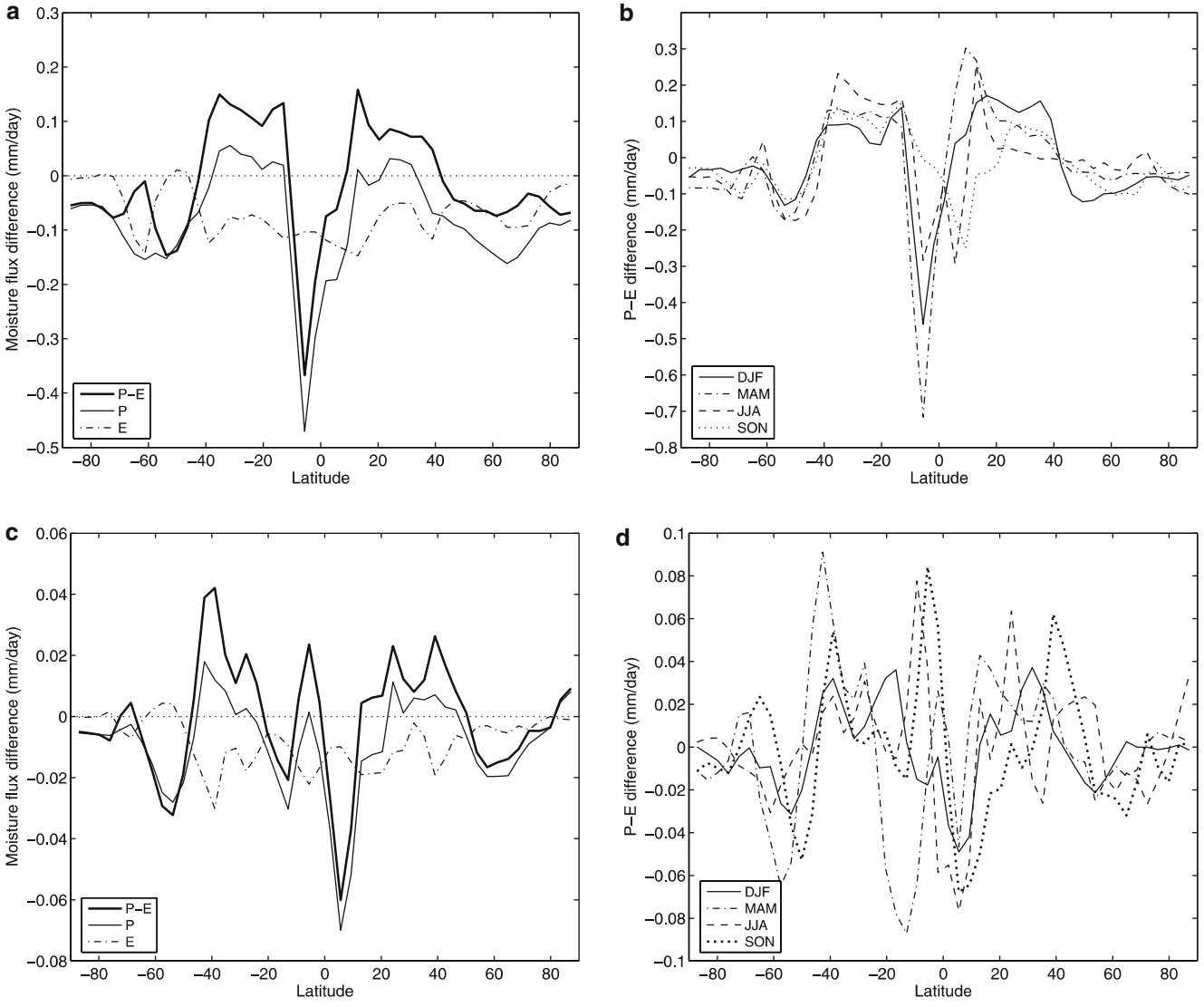

Fig. 4 Zonal mean surface moisture fluxes: **a** annual mean difference in $P - E$, P (precipitation), and E (evaporation) between the SMM and CTRL simulations; **b** seasonal mean $P - E$ differences between the SMM and CTRL simulations; **c** annual mean difference in $P - E$, P, and E between the TMM ensemble mean and the SMM simulation; and **d** seasonal mean $P - E$ differences between the TMM ensemble mean and the SMM simulation

of hydrological proxy records in these latitudes requires the consideration of both transient and stationary eddy transport processes. Note also that the contribution of the covariance term to the meridional moisture transport is small.

The decomposition of the time-mean component in TMM–SMM shows a rather different picture (Fig. 5d). In this case, the effects of specific humidity and circulation changes have comparable magnitudes although the structure is quite different. Note that the meridional structure of moisture transport change due to the specific humidity change is similar to SMM–CTRL (Fig. 5b). Again, the stationary eddy contribution is large in the Northern Hemisphere mid latitudes, and the covariance term is small. While it is tempting to further explore the mechanism of the circulation change, it is not efficiently described in the zonal mean analysis because the circulation change is not zonally symmetric. This point is addressed in the next section.

4.2 Horizontal moisture transport

The annual mean $P - E$ and vertically-integrated horizontal moisture transport for SMM–CTRL are shown in Fig. 6a, b, respectively. The $P - E$ difference reflects overall decreased precipitation in the tropics and high latitudes, and increased evaporation in the subtropics, as already seen in the zonal mean analysis. Main structures of $P - E$ in Fig. 6a are reproduced by the convergence of the horizontal moisture transport in Fig. 6b, ensuring the accuracy of the analysis. One of the most prominent features in Fig. 6b is reduced

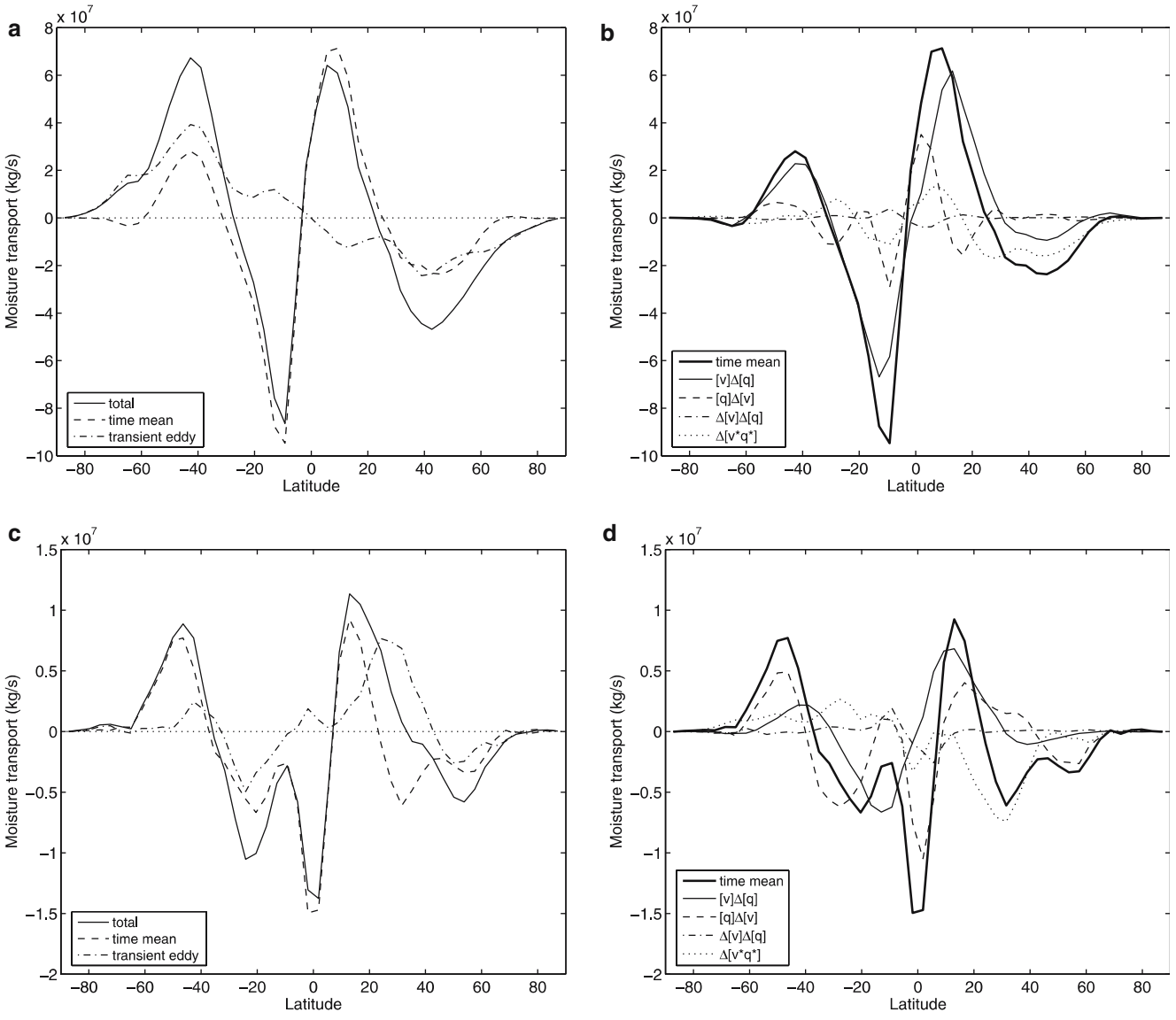

Fig. 5 Decomposition of zonally-integrated meridional moisture transport: **a** time-mean and transient eddy contributions in the difference between the SMM and CTRL simulations; **b** decomposition of the time-mean component in the difference between the SMM and CTRL simulations; **c** time-mean and transient eddy contributions in the difference between the TMM and SMM simulations; and **d** decomposition of the time-mean component in the difference between the TMM and SMM simulations. See Sect. 3 for details of the decomposition

westward and northeastward moisture transport in the tropics and Northern Hemisphere mid latitudes, respectively. The change in mid-latitude moisture transport is partly due to the reduced atmospheric water vapor content, but also consistent with weakening of Aleutian and Icelandic lows, particularly in winter, accompanied by elevated Arctic sea level pressure (i.e., low index state of Arctic Oscillation—AO). This negative AO is accompanied by a strong cooling in the tropical upper troposphere and hence smaller meridional temperature gradient at that level. Another feature is that large changes in moisture transport occur mainly over the ocean, consistent with Fig. 3b. Note that there is a strong reduction of moisture transport from the Atlantic to the Pacific in the tropics.

The total moisture transport change in Fig. 6b is decomposed into the time-mean and transient eddy components. The time-mean component for SMM–CTRL is further decomposed (cf. Sect. 3). Figure 7a–c, respectively, shows the effect of changes in specific humidity, circulation, and the covariance of the two on the time-mean component of the moisture transport. It is clear that the specific humidity change is a dominant factor for the change in the time-mean component in most regions. In the northeastern and southwestern tropical Pacific, however, effects of specific humidity and circulation changes have comparable magnitudes. Since the specific humidity decays exponentially with altitude in the atmosphere, the circulation-derived moisture transport changes in these region reflect a weakening of

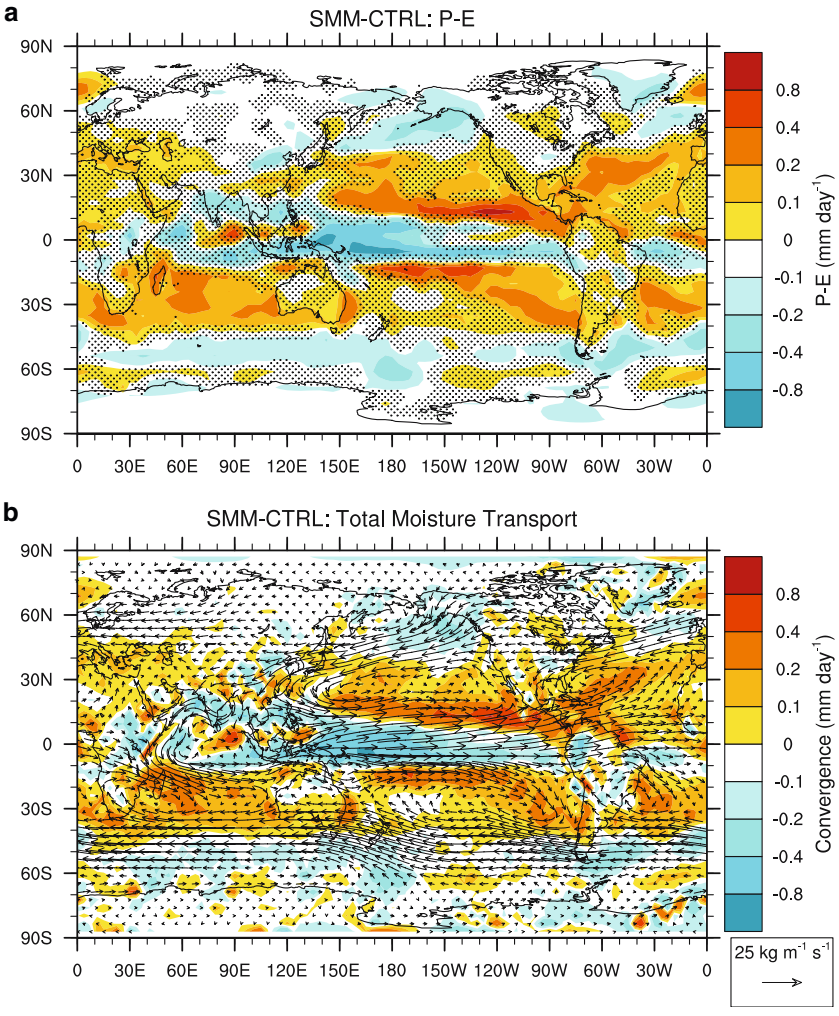

Fig. 6 The annual mean difference between the SMM and CTRL simulations: **a** $P - E$ (mm day^{-1}); and **b** vertically-integrated horizontal moisture transport (kg m^{-1} s^{-1}), and its convergence (mm day^{-1}). The locations, where the probability of falsely rejecting the null hypothesis is larger than 5% (Student's *t*-test), are stippled in **a**. Here the null hypothesis states that the means of the two simulations are equal. Note that small differences between $P - E$ in **a** and convergence in **b** are mainly due to the use of vertical and horizontal interpolations in calculating the convergence

trade winds, consistent with Fig. 5b. The contribution of the covariance term on the moisture transport is generally small. The specific humidity change contributes to the divergence of horizontal moisture transport, i.e., reduction in $P - E$, in the western tropical Pacific and the convergence in the eastern tropical Pacific. The circulation change contributes to the equatorial divergence and off-equatorial convergence in the Pacific. It is worth noting that the individual effects of specific humidity and circulation changes on the convergence counteract each other in some regions such as Africa, South America, and the Indian and subtropical Atlantic Oceans. This implies that any inferences from proxy records in these regions for the change in either specific humidity or circulation alone may result in the underestimation of the magnitude.

The annual mean $P - E$ and vertically-integrated horizontal moisture transport for TMM–SMM are shown in Fig. 8a, b, respectively. $P - E$ exhibits more zonally-asymmetric structure than SMM–CTRL. Somewhat similar to Fig. 6b, westward and eastward moisture transports are reduced in the tropics and mid latitudes, respectively. The magnitude of the changes is, however, 3–4 times smaller than SMM–CTRL. In contrast to SMM–CTRL, TMM–SMM does not exhibit changes in AO, and the change in mid-latitude moisture transport is not related to its phases. Again, the moisture transport from the Atlantic to the Pacific decreases.

The time-mean component for TMM–SMM is further decomposed (cf. Sect. 3). Figure 9a–c, respectively, shows the effect of changes in specific humidity, circulation, and the covariance of the two on the time-mean component of the moisture transport. In contrast to SMM–CTRL, the effect of circulation changes shows a comparable or even larger magnitude to the effect of specific humidity changes in many regions. The covariance term shows a relatively large contribution to the meridional moisture transport, causing a large moisture divergence in the western tropical Pacific and Indian Ocean. This implies that care must be exercised to attribute proxy records in these regions to the change in either specific humidity or circulation alone. Note that the contribution of the covariance term on the poleward moisture transport around 20° latitudes in the western tropical Pacific is counteracted by the equatorward moisture transport due to specific humidity change, resulting in little net meridional fluxes, as also seen in the next section in more detail.

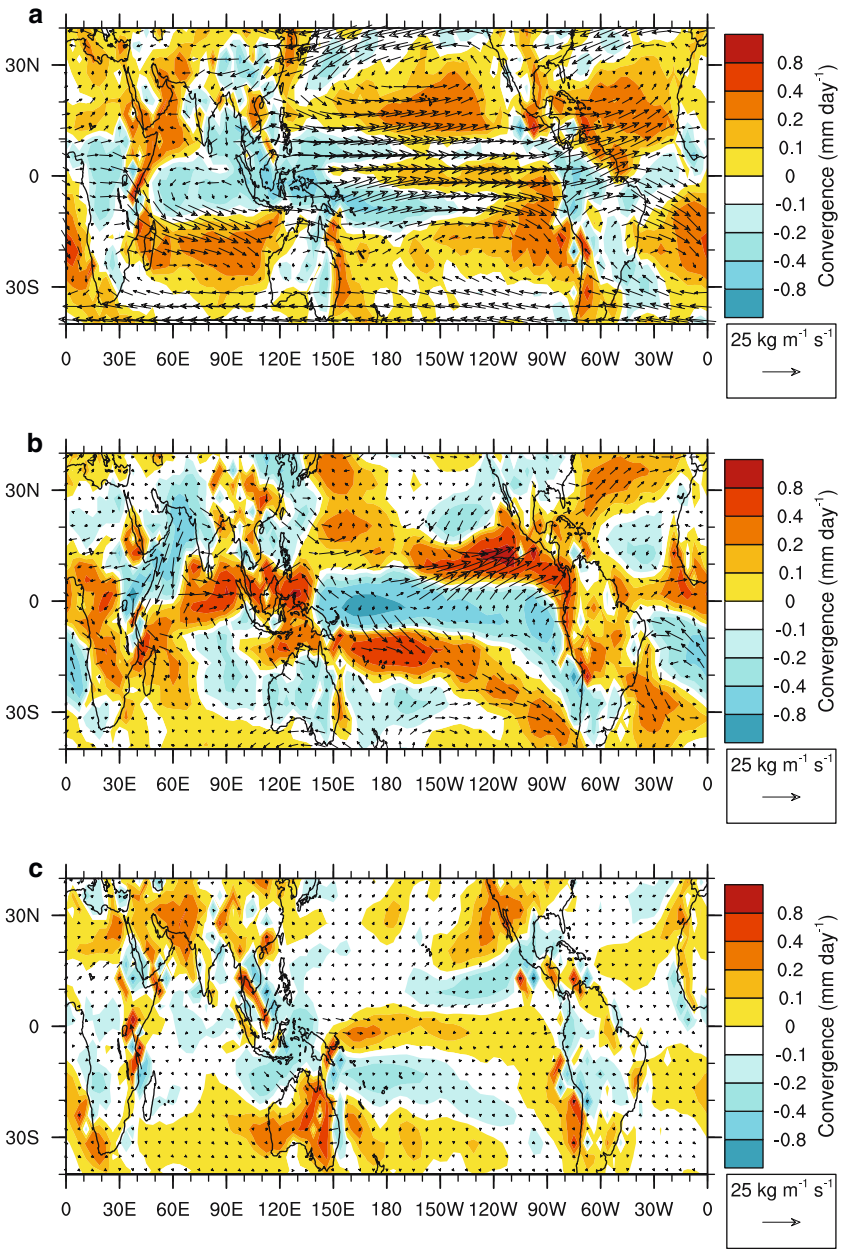

Fig. 7 Difference in the vertically-integrated time-mean component of the horizontal moisture transport between the SMM and CTRL simulations (kg m^{-1} s^{-1}), and its convergence (mm day^{-1}): **a** contribution of the specific humidity change, ($u\Delta q$, $v\Delta q$); **b** contribution of the circulation change, ($q\Delta u$, $q\Delta v$); and **c** covariance between specific humidity and circulation ($\Delta u\Delta q$, $\Delta v\Delta q$)

4.3 Moisture budget of western tropical Pacific

In order to help interpret the changes recorded in a proxy and to understand from where the moisture originates, a regional moisture budget analysis is conducted. The reconstructed sea surface temperature (SST) based on coral cores from the Great Barrier Reef, Australia, correlates reasonably well with the observed SST in a large region of western tropical Pacific (20°S–20°N, 120°E–170°W) over the past 120 years (Hendy et al. 2002). However, the extent to which the proxy data represent regional, larger scale salinity changes is not known. Nevertheless, in our analysis we choose the same region as taken for SST. Figure 10a, b shows the differences in sea surface temperature and salinity between the TMM ensemble mean and CTRL simulations. Large cooling and high salinity anomalies are seen in a large area of the western tropical Pacific. The proxy record exhibits more saline conditions during the Maunder Minimum (about 0.23 per mil. higher oxygen isotope ratio compared to the modern, 1950–1985 mean value). The current model is not capable of properly simulating the climate in the exact same location where the cores were extracted. For example, the grid point which contains the core location (18°S, 146°E) is defined as land in the model, and the land-sea mask or coastlines are different between the atmospheric and ocean model components due to the different resolution. Averaging the relatively large area avoids the "one-grid point problem" and has the advantage that the signal-to-noise ratio is expected to increase, and hence the results are less subject to internal model variability (Stott and Tett 1998).

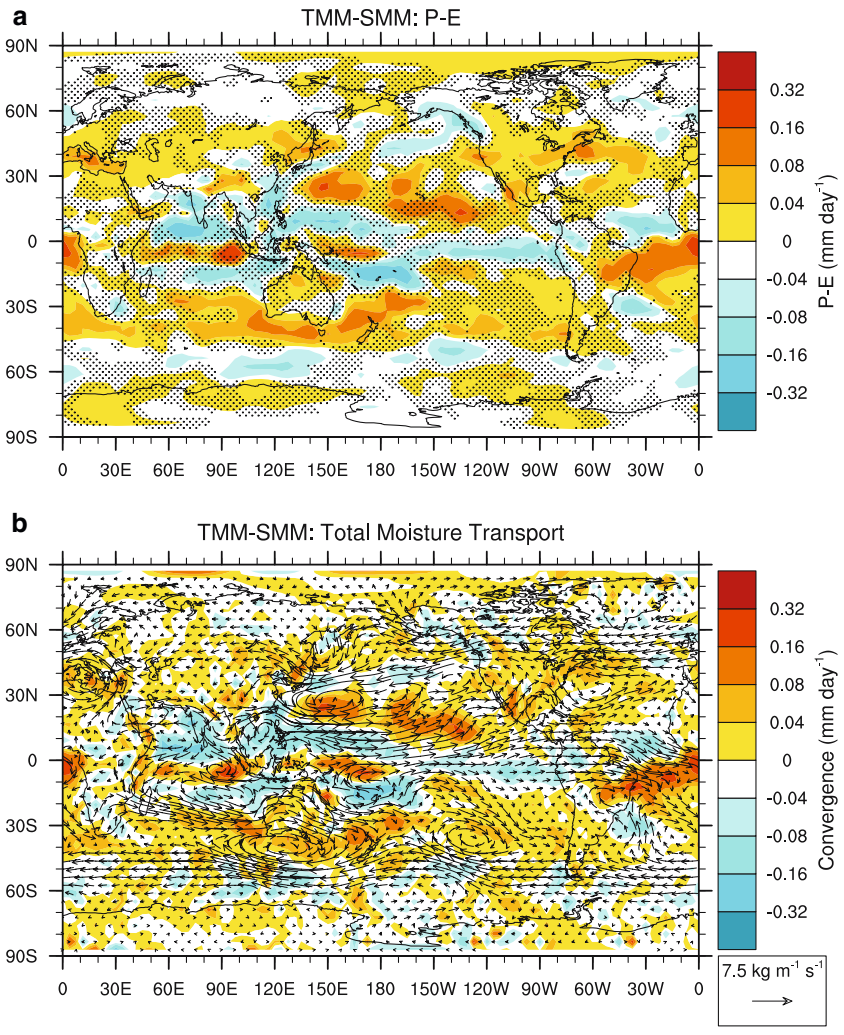

Fig. 8 The annual mean difference between the TMM ensemble mean and the SMM simulation: **a** $P - E$ (mm day^{-1}); and **b** vertically-integrated horizontal moisture transport (kg m^{-1} s^{-1}), and its convergence (mm day^{-1}). The locations, where mean changes are smaller than one standard deviation of intra-ensemble members, are stippled in **a**. Note that small differences between $P - E$ in **a** and convergence in **b** are mainly due to the use of vertical and horizontal interpolations in calculating the convergence

The SMM simulation exhibits higher salinity than the CTRL simulation by about 0.24 psu in the western tropical Pacific. The moisture budget of this region in the CTRL simulation and SMM–CTRL are summarized in Table 1. The analysis of surface moisture fluxes shows that the increased salinity in SMM–CTRL is explained by the decreased precipitation rather than the increased evaporation. The change in convergence of the lateral moisture fluxes is dominated by the increased net eastward moisture transport (or reduced westward moisture transport) at the eastern boundary of the region. This indicates that the proxy record likely represents zonal, rather than meridional, moisture transport changes. The large changes in zonal moisture transport at the eastern boundary of the region in SMM–CTRL is related to the dominance of this term in the CTRL simulation.

The decomposition of the moisture fluxes into the time-mean and transient eddy components shows that the convergence of zonal moisture fluxes is explained almost entirely by changes in the time-mean component. The change in the time-mean component of the zonal moisture transport at the eastern boundary of the region is quasi-symmetric about the equator as illustrated by a vertical profile (Fig. 11a and also Fig. 6b). The zonal moisture transport change is dominated by the contribution of specific humidity change with a small contribution of zonal wind change (Fig. 11b), consistent with Fig. 7a, b. The specific humidity change mainly occurs in the lower troposphere (Fig. 11c), which is expected from the fact that the water vapor is concentrated there in the present-day climate. The reduction of specific humidity is explained by the colder temperature in the SMM simulations relative to the CTRL simulations. Contrary to the specific humidity change, the zonal wind change is observed throughout lower- to mid-troposphere (Fig. 11d), which mainly reflects the weakening of trade winds in summer at this longitude as shown later.

The TMM ensemble simulations exhibit higher salinity than the SMM simulation by about 0.036 psu in the mean, with a standard deviation of about 0.025 psu, in the western tropical Pacific. Analyzing all ensemble members separately, each member shows higher salinity than the SMM simulation. Thus, the simulated salinity anomaly is an externally-forced signal rather than a mere coincidence. The analysis of surface moisture

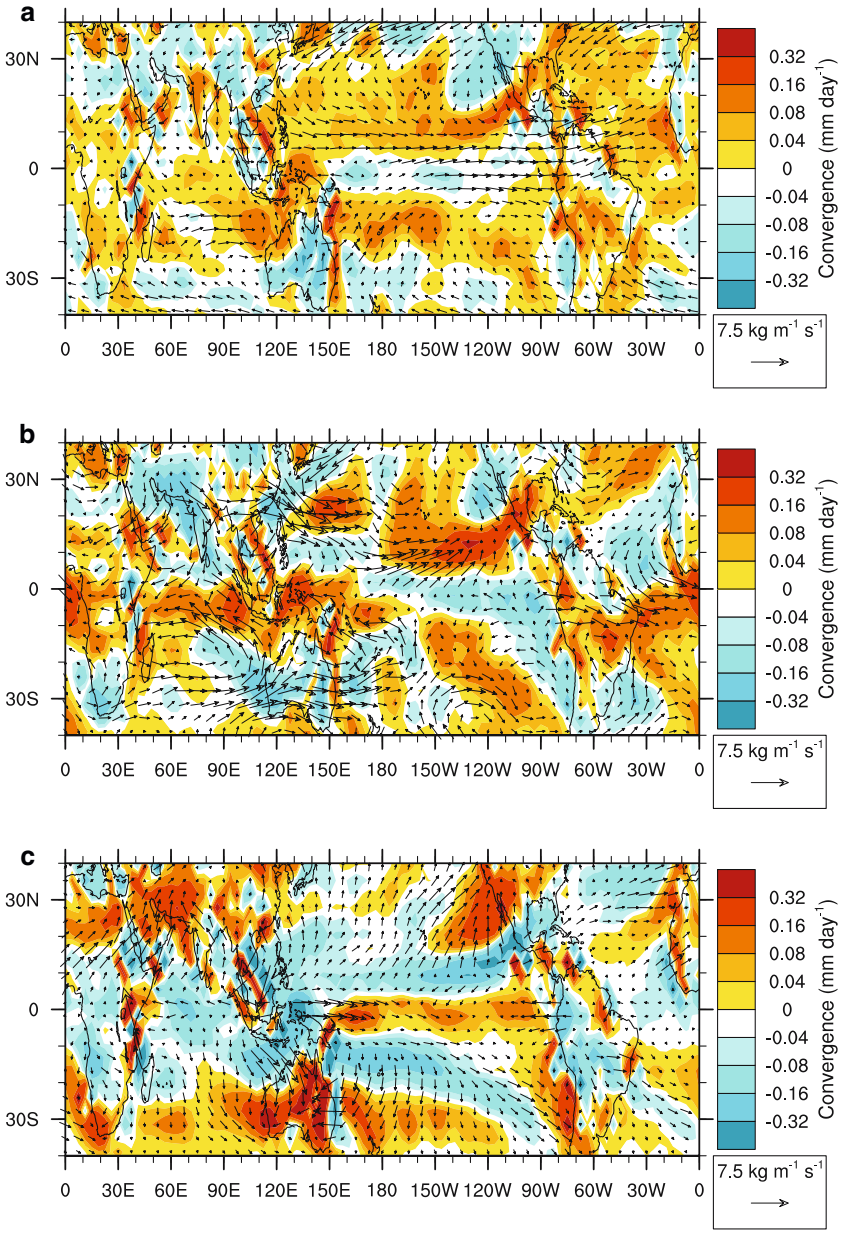

Fig. 9 Same as in Fig. 7 but for the difference between the TMM and SMM simulations

fluxes in the TMM ensemble mean shows that the increased salinity is explained by decreased precipitation rather than by increased evaporation (Table 2). It is also clear that the reduced horizontal moisture convergence is mainly due to the reduced convergence of zonal, rather than meridional, moisture transport. Furthermore, the change in the zonal convergence is caused by the reduced westward moisture transport at the eastern boundary of the region. All but one ensemble member show this behavior.

As in the case for SMM–CTRL, the decomposition of the moisture fluxes into the time-mean and transient eddy components shows that the convergence of zonal moisture fluxes is explained almost entirely by changes in the time-mean component. Changes in zonal moisture transport at the eastern boundary of the region is predominant in the northern half of the region from 0° to 20°N as illustrated by a vertical profile (Fig. 12a). This is in contrast to Fig. 11a in which the transport is equally contributed by the northern and southern half of the region. Therefore, we focus on the northern part of the selected region in the western tropical Pacific. The contribution of zonal wind changes to zonal moisture transport changes is larger than that of specific humidity changes (Fig. 12b). This is also in contrast to Fig. 11b, in which the specific humidity change makes a dominant contribution. The reduction of specific humidity occurs mainly in the lower troposphere, while the zonal wind change is seen throughout the lower- to mid-troposphere (Fig. 12c, d). The reduction of specific humidity is again explained by the colder temperature in the TMM simulations due to reduced solar irradiance and the presence

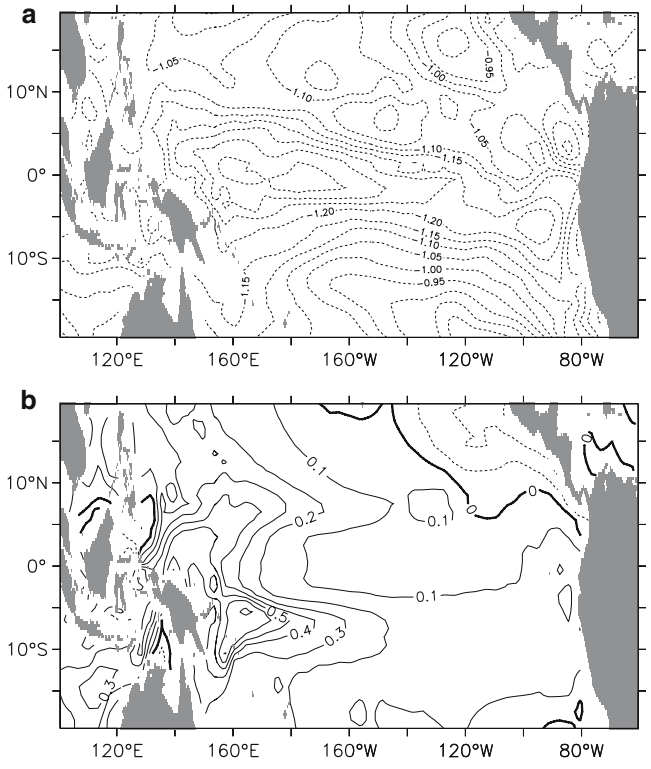

Fig. 10 Differences between the TMM ensemble mean and CTRL simulation: **a** sea surface temperature (°C) with a contour interval of 0.05°C; and **b** sea surface salinity with a contour interval of 0.1 psu. Negative contours are represented by *dashed lines*

of volcanic eruptions relative to the SMM simulation. The specific humidity change in TMM–SMM is much smaller than SMM–CTRL (Figs. 11c, 12c), consistent with much smaller temperature differences (Fig. 3a, c). Note that the similar magnitude of the trade wind changes at this longitude between Figs. 11d and 12d is due to the difference in the latitudinal extent in the meridional average.

It is shown that the zonal wind change at 170°W is a dominant factor in determining the moisture budget in TMM–SMM, whereas it plays only a minor role in SMM–CTRL. In order to obtain a complete picture of the hydrological response of the model, we further investigate the mechanism of the zonal wind changes.

Near-surface zonal wind at about 170°W shows the strongest changes in boreal summer for both SMM–CTRL and TMM–SMM. Figure 13a shows the difference in near-surface wind velocity superimposed on the vertical pressure velocity in August for SMM–CTRL. It is clearly depicted that the large zonal wind changes occur as a part of weakened trade winds: southwesterly anomaly for the northeasterly trade in off-equatorial northern tropical latitudes and northwesterly anomaly for the southeasterly trade in off-equatorial southern tropical latitudes. It also shows that the northern anomaly is larger. Figure 13b shows the difference in near-surface wind velocity and vertical pressure velocity in July for TMM–SMM. This figure exhibits similar features to Fig. 13a, i.e., weakening of trade winds and near-equatorial convergence, and increased downward wind velocity. However, the trade wind anomaly is only evident in the northern tropical latitudes.

The zonally-integrated streamfunction shows that the Hadley circulation weakens in TMM–SMM annual mean in the northern cell, although changes in the southern cell are relatively noisy (not shown). The weakening of the ascending branch of the Hadley circulation near 5–15°N was thought to be associated with the weakening of trade winds in Yoshimori et al. (2005). However, weaker trade winds in the tropical Pacific during summer do not necessarily mean that the zonal-mean Hadley circulation is weaker. In SMM–CTRL, for example, the Hadley circulation is stronger in summer, while the northern cell is weaker in the annual mean. One complication is that the zonal-mean picture does not necessarily represent the tropical Pacific circulation alone. More importantly in this case, however, changes in vertical velocity in Fig. 13 indicate that the weakening of trade winds is linked to the decrease and increase of convective activity in western equatorial Pacific and northeastern tropical Pacific, respectively. This shift is consistent with changes in SST in such a way that the convection shifts from the region of stronger cooling near the equator to less cooling off the equator (Fig. 10a, and also see ocean-only in Fig. 3a, c). Changes in convective region are accompanied by changes in low-level convergence, i.e., trade winds (cf. Lindzen and Nigam 1987). The SST responses to external forcing are, however, possibly model-dependent (Collins and The CMIP Modelling Groups 2005). As the moisture budget in TMM–CTRL is dominated by the effect of specific humidity change, we consider the main result to be robust with respect to SST pattern changes.

The west–east temperature gradient in the equatorial Pacific decreases in SMM–CTRL as strongly reflected in TMM–CTRL in Fig. 10a, but the spatial pattern does not suggest a linkage to ENSO variability. The ensemble mean west–east temperature gradient in the equatorial Pacific increases in TMM–SMM, but this is not a robust response as three members show decreases, two members show increases, and one member does not show a monotonic gradient. Note also that the model exhibits too regular ENSO cycles, i.e., strong 2-year periodicity (e.g., NINO3 index), and this behavior does not change in any of the experiments. This is a deficiency of the model in that it does not produce a realistic broad-band ENSO variability, and the model ENSO seems to be rather insensitive to the background climate change imposed here. This point needs to be verified or falsified by models with more realistic ENSO simulations.

4.4 Comparisons with hydrological proxy records

It is of great interest to examine model-simulated hydrological response with other available hydrological proxy records. We restrict our comparisons to relatively

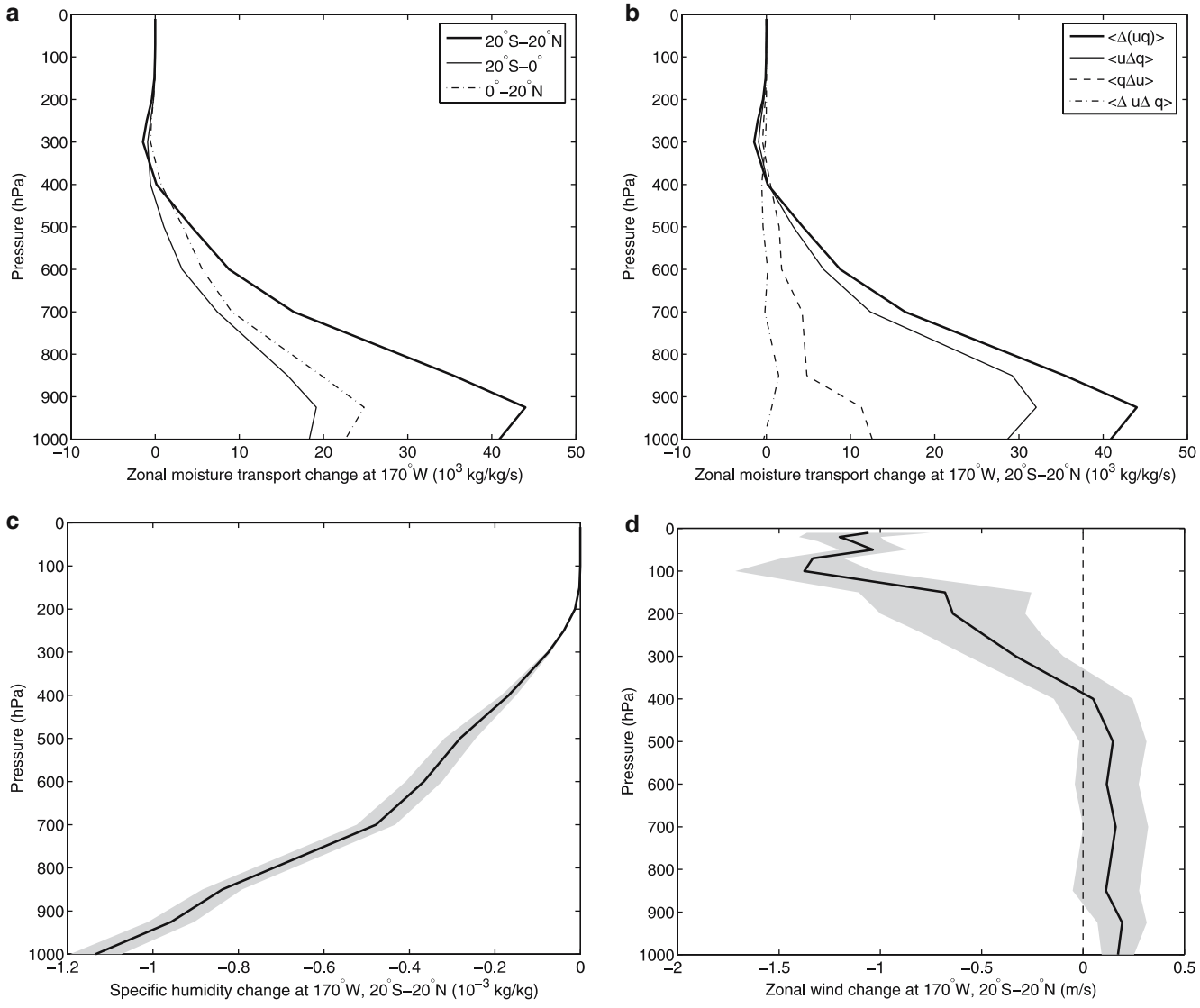

Fig. 11 Vertical profiles of the difference between the SMM and CTRL simulations at the eastern boundary of the western tropical Pacific region: **a** zonal moisture flux in northern and southern parts of the region; **b** decomposition of the zonal moisture flux (here the angle bracket, $< >$, denotes meridional integration between 20°S and 20°N); **c** specific humidity changes averaged between 20°S and 20°N; and **d** zonal wind changes averaged between 20°S and 20°N. *Shadings* represent 95% confidence intervals for the estimate of the mean differences calculated with the Welch approximation

low-latitude proxy records that cover at least part of the Maunder Minimum period. In Fig. 6a, the locations, where the externally forced annual mean $P - E$ signal is not statistically distinguishable from the model-generated internal variability, are stippled. In Fig. 8a, on the other hand, the locations, where the externally forced signal is not distinguishable from the intra-ensemble spread, are stippled. Although not shown, precipitation and soil moisture are also examined in the same way when appropriate for some proxy records.

Summer drought area fraction in the western half of the USA based on tree-ring records indicates relatively wet conditions in the seventeenth and eighteenth centuries and increasing aridity in the twentieth century (Cook et al. 2004). Although not limited to summer, precipitation reconstructions of northwest New Mexico (October–July), southern Colorado Plateau (annual mean), and Wyoming (annual mean) seem to suggest, on the other hand, drier conditions during the Maunder Minimum compared to the last couple of decades (Grissino-Mayer 1996; Gray et al. 2004; Salzer and Kipfmueller 2005). Also, annual mean precipitation reconstruction from Nevada indicates a distinct dryness during the Maunder Minimum (Hughes and Graumlich 1996). While increased $P - E$ in the western USA in TMM–SMM (annual mean as well as summer) is somewhat consistent with Cook et al. (2004), the difference is not statistically significant in SMM–CTRL. Similarly, soil moisture suggests wetter conditions in TMM–SMM, but it does not stand out for

Table 2 Difference in annual moisture budget in the western tropical Pacific between the TMM and SMM simulations (10^6 kg s^{-1})

Variable	Mean	STD
Precipitation (P)	−17.2	7.8
Evaporation (E)	−4.2	1.6
$P - E$	−12.9	6.7
F_W	9.4	9.9
F_E	**19.4**	9.1
F_S	−6.2	3.0
F_N	−2.6	3.4
$F_W - F_E$	−10.0	7.7
$F_S - F_N$	−3.6	4.8
$F_W - F_E + F_S - F_N$	−13.6	6.6

The mean and standard deviation (STD) are calculated for the difference between the TMM ensemble members and the SMM simulation. The dominant term in the lateral moisture fluxes is highlighted by bold

SMM–CTRL because areas of wetter and drier conditions approximately cancel out when averaged over western half of the USA.

Lake sediment records from tropical east Africa and Yucatan Peninsula in Mexico both show wetter conditions during the period of reduced solar activity including Maunder Minimum (Verschuren et al. 2000; Hodell et al. 2001) while winter precipitation reconstructions based on tree-ring record from Mexico do not show such changes during the Maunder Minimum (Díaz et al. 2002; Cleaveland et al. 2003). Both $P - E$ and soil moisture difference in these two locations in TMM–SMM is within the range of internal variability. The marine sediment record from Cariaco Basin in the southern Caribbean implies stronger trade-wind-driven upwelling (Black et al. 1999), and reduced runoff and precipitation during LIA with an amplification during the Maunder Minimum (Haug et al. 2001, 2003). Simulated changes (SMM–CTRL) are inconsistent with these changes. A marine sediment record from Oman margin in Arabian Sea exhibits increasing strength of Asian southwest monsoon from the seventeenth to twentieth centuries (Anderson et al. 2002; Gupta et al. 2003). These records are consistent with the simulated weaker monsoon and reduced precipitation in India, particularly in summer, in both SMM–CTRL and TMM–SMM (not shown but the trace can be seen in the annual mean, Figs. 6b, 7b). Ice core records from Quelccaya in Peru show increased net accumulation and hence precipitation between 1500 and 1720, followed by a dry period from 1720 to 1860 (Thompson et al. 1985). There is no such indication in our simulations, but it should be noted that the model resolution is far too coarse to expect a reasonable representation of climate in high altitude regions such as the Andes. Furthermore, it is debated whether the oxygen isotope record from tropical ice caps is a proxy for temperature or rather precipitation (Thompson et al. 1986; Hoffmann et al. 2003). Assuming the latter, the record indicates a much longer wet period from 1530 to 1900 (Hoffmann 2003). There are also precipitation reconstructions from other regions such as China, Mongolia, Turkey, Iowa, and Southeastern USA, but these reconstructions do not show significant changes during the Maunder Minimum relative to the long-term pre-industrial or industrial means (Hughes et al. 1994; Pederson et al. 2001; D'Arrigo and Cullen 2001; Touchan et al. 2003; Cleaveland and Duvick 1992; Stahle and Cleaveland 1992).

The evaluation of the model performance by these comparisons are inconclusive for several reasons. Firstly, as discussed in more detail in the next section, the uncertainty in magnitude and spatial pattern of forcing history, and its representation in the model is not negligible. More constraints are needed to attribute the similarities and differences of model-data comparisons to the model performance. Secondly, the model-simulated responses in many locations are generally indistinguishable from the internal variability, not only for TMM–SMM but also for SMM–CTRL. Therefore, it is necessary to obtain some idea about whether proxy records represent local or large scale signals to evaluate the signal-to-noise ratio in the model. In most cases, however, it is not yet clear for which spatial extent the reconstructed hydrological data are representative. This is partly due to the sparseness of the global hydrological proxy records. Establishing of a dense network of proxy records and synthesized dataset would be desirable.

5 Discussion

In this study as well as other modeling studies on the climate of the last millennium, uncertainties reside in every step taken: forcing, model, and climate reconstructions. It is important to stress such uncertainties, because the results are sensitive to them. In particular, the effect of specific humidity on the moisture convergence is closely related to the surface air temperature via the Clausius–Clapeyron equation. We explore the major uncertainties in the following.

In our forcing data, the effect of some forcing agents such as changes in ozone and aerosol concentrations are not included. According to the IPCC TAR estimate of the global-mean radiative forcing between years 2000 and 1750 (Ramaswamy et al. 2001), it appears that at least part of these forcings cancel out owing to positive (e.g., tropospheric ozone and black carbon) and negative (e.g., sulfate aerosols) forcing agents. Due to the large uncertainty in the estimate, however, even the sign of the sum of the forcing due to ozone and the direct effect of tropospheric aerosols is not clear. The IPCC TAR estimate of the radiative forcing for the indirect effect of tropospheric aerosols for the same period ranges from -2 to 0 Wm^{-2} (see also Anderson et al. 2003). As pointed out by Rind et al. (2004), the magnitude of the effect of tropospheric aerosols, especially the indirect effect, could have a profound influence on the total radiative forcing between the Maunder Minimum and

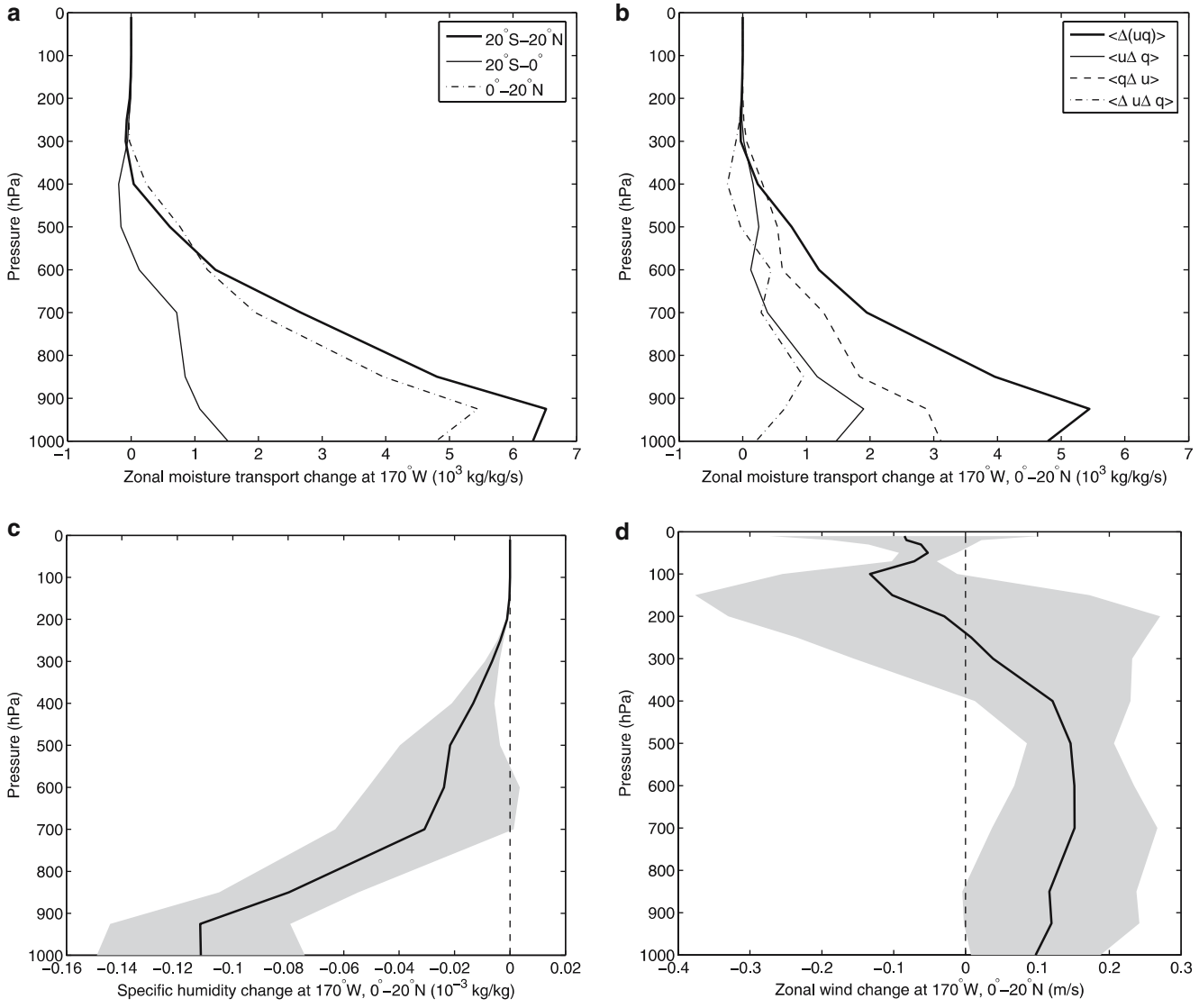

Fig. 12 Vertical profiles of the difference between the TMM and SMM simulations at the eastern boundary of the western tropical Pacific region: **a** zonal moisture flux in northern and southern parts of the region; **b** decomposition of the zonal moisture flux (here the angle bracket, $< >$, denotes meridional integration between 0° and 20°N); **c** specific humidity changes averaged between 0° and 20°N; and **d** zonal wind changes averaged between 0° and 20°N. *Shadings* represent ± 1 standard deviation of the TMM ensemble members centered on its mean

present-day, and hence our understanding of the climate during that period. Hansen et al. (2005b) estimated the radiative forcing as 1.51 Wm^{-2} for the same period as IPCC TAR without solar and volcanic forcing, and 1.54 Wm^{-2} when the "efficacy" of each forcing agent in changing the global-mean surface air temperature is taken into account. Therefore, the magnitude of the GHG radiative forcing of about 2.2 Wm^{-2} imposed for SMM–CTRL in the present study might be overestimated when other forcing agents are ignored, and result in producing a cold-biased climate. If the estimate of Hansen et al. (2005b) is correct, the current model would overestimate the cooling by as much as 0.5°C. In addition, regional influence of the ignored forcings could be much larger, particularly over land. As stated in Sect. 1, Rind et al. (2004) updated the uncertainty of about a factor of 8 in solar forcing (0.05–0.4% or 0.12–0.96 Wm^{-2}, assuming TSI of 1,367 Wm^{-2} and the planetary albedo of 0.3) during the Maunder Minimum relative to the present. While we note that the magnitude of solar radiative forcing of 0.33 Wm^{-2} imposed for SMM–CTRL is very close to the value of 0.30 Wm^{-2} estimated between years 2000 and 1750 by Hansen et al. (2005b), recent reconstructions tend to favour smaller values. When the magnitude of total forcing in SMM–CTRL is considered, our forcing of about 2.5 Wm^{-2} is less than, but close to, the upper limit of the uncertainty range in the estimated effective radiative forcing (1.80 ± 0.85 Wm^{-2}) for the period between years 2003 and 1880 by Hansen et al. (2005a).

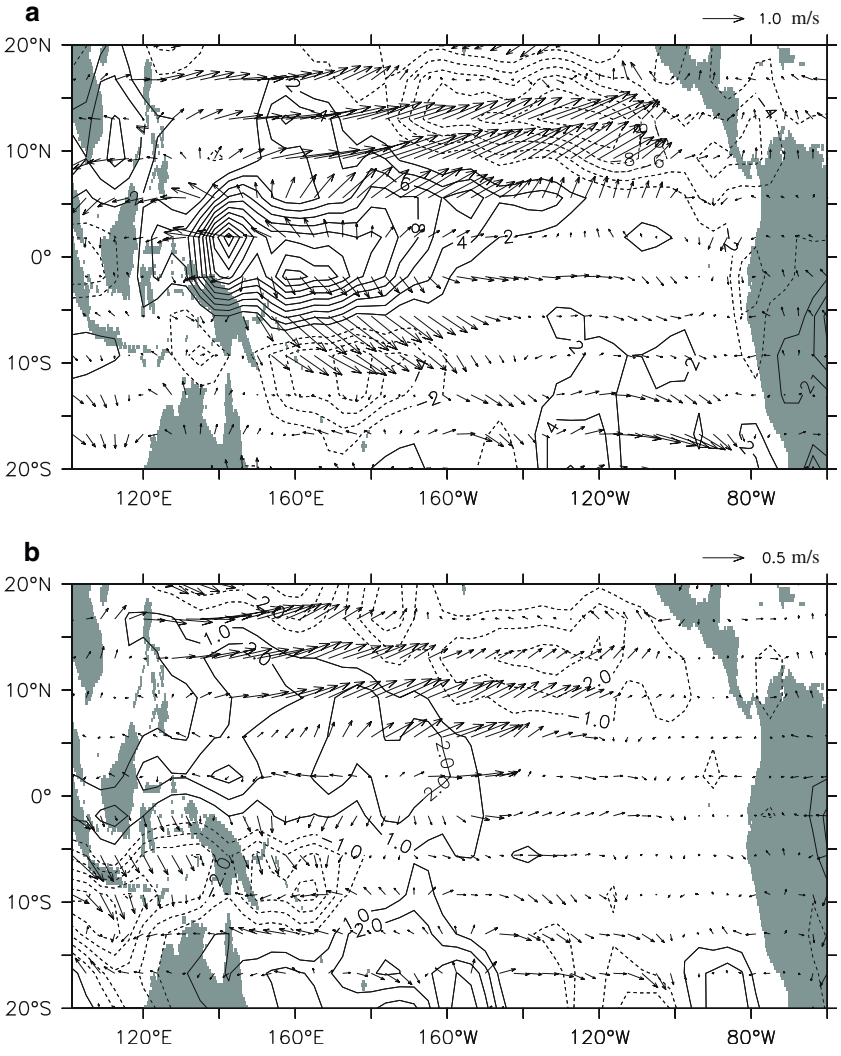

Fig. 13 **a** Near-surface wind velocity indicated by the *arrows* (m s^{-1}) and vertical pressure velocity averaged over the lower troposphere from 1,000 to 500 hPa with a contour interval of 2.0 ($\times 10^{-3}$ Pa s^{-1}) in the difference between the SMM and CTRL simulations in August. Note that vertical pressure velocity directs downward with positive values. Zero contours are omitted; **b** same as in **a** but for the difference between the TMM ensemble mean and the SMM simulation in July with a contour interval of 1.0 ($\times 10^{-3}$ Pa s^{-1})

There are at least two types of uncertainties in the model simulations. In both the CTRL and SMM simulations, the analyzed data are taken from the quasi-steady state under the perpetual AD 1990 and 1640 forcing, and the TMM simulations start from the quasi-steady state of the SMM simulation. Therefore, SMM–CTRL and hence TMM–CTRL contains the so-called "committed" climate change which has not been experienced by the real climate system. Based on the radiative imbalance, Hansen et al. (2005a) estimated that the earth is presently committed to warm up by about 0.6°C even if the atmospheric composition and other climate forcings remain the same. Similarly, Weaver et al. (2000) demonstrated that a transient simulation, starting from 6,000 years ago, is about 0.5°C colder today than the equilibrium present-day simulation. This means that the use of perpetual AD 1990 simulation as a reference introduces a bias into the results. It is, therefore, possible that SMM–CTRL and hence TMM–CTRL exaggerate the climate difference between the Maunder Minimum and present-day recorded in proxy records by including the committed climate change. Similarly, the forcing prior to AD 1640, which is missing in the simulations, could have an impact on the proxy records after that time. The exploration of this type of uncertainty is not done in the present study and left for future studies. The multi-century transient simulations would greatly reduce this error, but still "defining suitable initial conditions is extremely tricky and laborious" as stated in Schmidt et al. (2004). Another type of uncertainty, not unique to the time period of interest here, is the climate sensitivity of the model. Crowley (2000), setting the climate sensitivity of 2°C for a doubling of CO_2, demonstrated that an energy balance model reproduces some of the reconstructed global temperature records over the last millennium fairly well. Shindell et al. (2001b), on the other hand, demonstrated that Northern Hemisphere regional climate change during the Maunder Minimum is captured via dynamical feedback using a GCM with the climate sensitivity of 4.5°C. The IPCC TAR estimated the approximate range of climate sensitivity as 1.5–4.5°C, although Knutti et al. (2002; 2006) suggest the range could be larger. A rough estimate of the climate sensitivity of the present model is about 2.5°C, and

it is possible that the model produces a slightly conservative response in terms of temperature. Note that the uncertainties associated with commitment and climate sensitivity are not independent because the commitment depends on the climate sensitivity (Hansen et al. 2005a).

As stated briefly in Sect. 1, the hemispheric-scale temperature reconstructions do not agree with respect to the low-frequency or multi-centennial scale variability. While Moberg et al. (2005) argue that high temperature similar to the twentieth century occurred in the eleventh century, Osborn and Briffa (2006) seem to suggest that the twentieth century warming stands out over the last 1,200 years. The three different reconstructions suggest about −0.3°C (Mann et al. 1999), −0.7°C (Esper et al. 2002), and −0.6°C (Moberg et al. 2005) for the Northern Hemisphere temperature during the Maunder Minimum relative to the 1960–1990 mean. As the Northern Hemisphere temperature around the year 1990–2000, which is close to our control simulation, is roughly 0.4°C warmer than the reference period of 1960–1990 (Jones and Mann 2004, Fig. 2), these three reconstructions seem to suggest that the Northern Hemisphere mean cooling for TMM–CTRL should be about 0.7–1.1°C. However, the uncertainty range suggested by individual reconstructions are also large, and even larger than suggested by the spread of these reconstructions. For example, the uncertainty range ($\pm$ 2σ errors) is about 0.5°C in Mann et al. (1999) during the Maunder Minimum on average, and much larger in Esper et al. (2002, Fig. 3). Note that it is pointed out by Osborn and Briffa (2006) that these uncertainty estimates are either incomplete or probably underestimated. Nevertheless, the simulated cooling in the mean TMM–CTRL is 1.8°C, and appears to be too large. This large cooling is probably a result of the relatively large forcing imposed and the inclusion of committed climate change in the analysis. The removal of committed climate change of 0.6°C brings the value much closer to the reconstructions, illustrating the limitation of the experiments focused only on a certain time window.

Keeping these uncertainties in mind, it is demonstrated that the decomposition of moisture fluxes into the contributions of local specific humidity and wind velocity changes is useful to obtain an idea of dominant mechanisms controlling hydrological response patterns. In the present analysis, the local correlation between specific humidity and wind velocity is also taken into account. Along with the strength of this approach, there is a potential caveat. The distribution of atmospheric water vapor is undoubtedly linked to large-scale atmospheric circulation. Hence, local specific humidity changes may be indirectly controlled by the large-scale or remote circulation changes as well as local temperature changes. Therefore, these two contributions are not independent and cannot be separated completely. Nevertheless, the notion that local specific humidity strongly depends on the local temperature associated with the Clausius–Clapeyron relation, and that itself has a large potential influence on proxy records, is important. In other words, hydrological proxy records contain both dynamical and thermal influences. Therefore, they should not be interpreted, by themselves, as proxies for the past circulation changes. By the same token, circulation changes could be masked by the specific humidity effect in proxy records. In the zonal mean analysis, for example, if proxy records suggest wetter conditions in the tropics and drier conditions in the subtropics in the colder climate, it is possible that they are strongly linked to the change in the strength of the Hadley circulation. In such a case, the inferred circulation change could be even underestimated by the counteracting effect of the specific humidity change on the meridional moisture transport. By examining carefully such a complication, we would obtain a clearer picture of changes in the past hydrological cycle and atmospheric circulation.

A hypothesis is given in the present study with respect to the interpretation of the proxy record from the western tropical Pacific: higher salinity during the Maunder Minimum compared to the late nineteenth and twentieth centuries can be explained, for a large part, by the reduction in precipitation caused by the reduced atmospheric moisture content in the tropical Pacific in the cold climate. One important aspect yet to be explored is that the record also shows continuous high salinity after the Maunder Minimum to the mid-nineteenth century when the temperature proxy from the same core indicates warm conditions. This absence of cooling is argued, by Mann et al. (2005), as supporting evidence of an increased El Niño-like state responding to the reduced solar and increased volcanic activity (cf. Adams et al. 2003). While the reason for the inconsistency between the Maunder Minimum and the following two centuries is not clear, it is possible that different processes are responsible for the salinity changes in these two periods. Our simulations only cover the Maunder Minimum period, and hence the interpretation on this aspect is limited. The multi-century transient simulations are, however, currently underway.

6 Summary

Three types of experiments are carried out using a coupled AOGCM: a present-day control, a perpetual AD 1640, and an ensemble of six transient Maunder Minimum (AD 1640–1715) simulations. Changes in the hydrological cycle are described in terms of meridional distribution of moisture, horizontal moisture transport, and moisture budget of a specific region. The mechanisms for the simulated difference between precipitation and evaporation or convergence of moisture transport are investigated by decomposing it into various contributions such as transient eddy, specific humidity change, circulation change, and the covariance of specific humidity and circulation. Most results are presented as the difference between the long-term pre-industrial mean and the present-day (SMM–CTRL), and the difference between the Maunder Minimum and the pre-industrial

mean (TMM–SMM). The link between model output and proxy records can be sensitive to uncertainties in forcing reconstructions, climate sensitivity and climate reconstructions, and performed time-window experiments. Thus, the following conclusions are not definitive, but they have important implications for the interpretation of the low-latitude hydrological proxy records possibly beyond the Maunder Minimum period:

- The $P - E$ change in TMM–SMM is an order of magnitude smaller than in SMM–CTRL. Therefore, the change from the Maunder Minimum to the present-day reconstructed from proxy data are expected, to first order, to reflect the response of well-mixed GHG forcing (SMM–CTRL).
- The zonal mean analysis reveals that it is difficult to infer the change in the Hadley circulation solely from proxy records, because the thermal influence on $P - E$ is large.
- The analysis of horizontal moisture transport, for the difference between the Maunder Minimum and the present-day, shows that zonal transport is generally large particularly in the tropics. Also, the convergence of moisture transport in low latitudes is affected by both specific humidity and circulation changes.
- The moisture budget analysis in the western tropical Pacific reveals that the divergence of moisture transport, for the difference between the Maunder Minimum and the present-day, is caused mainly by the reduction of westward moisture influx from the east. The reduction of zonal influx is mainly due to the specific humidity change.
- Although the model simulation captures the Asian southwest monsoon response indicated by proxy records, comparisons with proxy records in other regions do not provide further confidence to the model simulations. Reduction of forcing uncertainty and synthesis of the hydrological proxy data are needed.

Due to the rich spatial variations in hydrological response, moisture sensitive proxy records potentially offer a good test for the performance of climate models. Climate models, on the other hand, offer an aid for the interpretation of such proxy records. Although both applications are severely limited by the existence of several uncertainty factors, with enhanced model-proxy data studies we will obtain more insight into the past and potential future hydrological changes.

Acknowledgments We are indebted to NCAR for their continuous effort in developing the model and making it available to the community. We are grateful for authors of cited reconstructions in making their data available to the community (http://www.ncdc.noaa.gov/paleo/paleo.html). Developers of freely available softwares, SCRIP, NCL and Ferret, are also acknowledged. This work is supported by the National Centre of Competence in Research (NCCR) Climate funded by the Swiss National Science Foundation. A substantial part of the computations was made on IBM Power 4 at the Swiss National Supercomputing Centre (CSCS) in Manno. TFS acknowledges support by IPRC and A. Timmermann during a sabbatical visit to IPRC in 2006. This is IPRC publication #381 and SOEST #6762. We thank two anonymous reviewers whose comments helped to clarify the text and to greatly improve the manuscript.

References

Adams JB, Mann ME, Ammann CM (2003) Proxy evidence for an El Niño-like response to volcanic forcing. Nature 426(6964):274–278

Anderson DM, Overpeck JT, Gupta AK (2002) Increase in the Asian southwest monsoon during the past four centuries. Science 297(5581):596–599

Anderson TL, Charlson RJ, Schwartz SE, Knutti R, Boucher O, Rodhe H, Heintzerberg J (2003) Climate forcing by aerosols—a hazy picture. Science 300(5622):1103–1104

Andronova NG, Rozanov EV, Yang F, Schlesinger ME, Stenchikov GL (1999) Radiative forcing by volcanic aerosols from 1850 to 1994. J Geophys Res 104(D14):16807–16826

Black DE, Peterson LC, Overpeck JT, Kaplan A, Evans MN, Kashgarian M (1999) Eight centuries of North Atlantic ocean atmosphere variability. Science 286(5445):1709–1713

Bradley RS, Jones PD (1993) 'Little Ice Age' summer temperature variations: their nature and relevance to recent global warming. Holocene 3(4):367–376

Bradley RS, Briffa KR, Cole J, Hughes MK, Osborn TJ (2003) The climate of the last millennium. In: Alverson K, Bradley RS, Pedersen TF (eds) Paleoclimate, global change and the future. Springer, Berlin Heidelberg New York, pp 105–141

Broecker WS (2000) Was a change in thermohaline circulation responsible for Little Ice Age? Proc Natl Acad Sci USA 97(4):1339–1342

Cleaveland MK, Duvick DN (1992) Iowa climate changes analyzed with tree rings A.D. 1640 to 1982. Water Resour Res 28(10):2607–2615

Cleaveland MK, Stahle DW, Therrell MD, Villanueva-Diaz J, Burns BT (2003) Tree-ring reconstructed winter precipitation and tropical teleconnections in Durango, Mexico. Clim Change 59(3):369–388

Clement AC, Hall A, Broccoli AJ (2004) The importance of precessional signals in the tropical climate. Clim Dyn 22(4):327–341

Collins M, The CMIP Modelling Groups (2005) El Niño- or La Niña-like climate change. Clim Dyn 24(1):89–104

Cook ER, Woodhouse CA, Eakin CM, Meko DM, Stahle DW (2004) Long-term aridity changes in the western United States. Science 306(5698):1015–1018

Crowley TJ (2000) Causes of climate change over the past 1000 years. Science 289(5477):270–277

Cubasch U, Voss R, Hegerl GC, Waszkewitz J, Crowley TJ (1997) Simulation of the influence of solar radiation variations on the global climate with an ocean-atmosphere general circulation model. Clim Dyn 13(11):757–767

D'Arrigo R, Cullen HM (2001) A 350-year (AD 1628–1980) reconstruction of Turkish precipitation. Dendrochronologia 19(2):169–177

Devore JL (1987) Probability and statistics for engineering and the sciences, 2nd edn. Brooks/Cole Pub. Co., Monterey, 672pp

Díaz SC, Therrell MD, Stahle DW, Cleaveland MK (2002) Chihuahua (Mexico) winter-spring precipitation reconstructed from tree-rings, 1647–1992. Clim Res 22:237–244

Eddy JA (1976) The Maunder Minimum. Science 192(4245):1189–1202

Esper J, Cook ER, Schweingruber FH (2002) Low-frequency signals in long tree-ring chronologies for reconstructing past temperature variability. Science 295(5563):2250–2253

Folland CK, Karl TR, Christy JR, Clarke RA, Gruza GV, Jouzel J, Mann ME, Oerlemans J, Salinger MJ, Wang SW (2001) Observed climate variability and change. In: Houghton JT, Ding Y, Griggs DJ, Noguer M, van der Linden PJ, Dai X, Maskell K, Johnson CA (eds) Climate change 2001: the scientific basis, Chap

2. Cambridge University Press, Cambridge, pp 99–181, contribution of Working Group I to the Third Assessment Report of the Intergovenmental Panel on Climate Change, 881pp

Genfo ADD, Lacis AA, Ruedy RA (1991) Simulations of the effect of a warmer climate on atmospheric humidity. Nature 351:382–385

Gray ST, Fastie CL, Jackson ST, Betancourt JL (2004) Tree-ring-based reconstruction of precipitation in the Bighorn Basin, Wyoming, since. J Climate 17(19):3855–3865

Grissino-Mayer HD (1996) A 2129 year annual reconstruction of precipitation for northwestern New Mexico USA. In: Dean JS, Meko DM, Swetnam TW (eds) Tree rings, environment, and humanity. Radiocarbon 1996. The Univeristy of Arizona, Tucson, pp 191–204

Gupta AK, Anderson DM, Overpeck JT (2003) Abrupt changes in the Asian southwest monsoon during the Holocene and their links to the North Atlantic ocean. Nature 421(6921):354–357

Hansen J, Sato M, Nazarenko L, Ruedy R, Lacis A, Koch D, Tegen I, Hall T, Shindell D, Santer B, Stone P, Novakov T, Thomason L, Wang R, Wang Y, Jacob D, Hollandsworth S, Bishop L, Logan J, Thompson A, Stolarski R, Lean J, Willson R, Levitus S, Antonov J, Rayner N, Parker D, Christy J (2002) Climate forcings in Goddard Institute for Space Studies SI2000 simulations. J Geophys Res 107(D18):4347. DOI:10.1029/2001JD001143

Hansen J, Nazarenko L, Ruedy R, Sato M, Willis J, Genio AD, Koch D, Lacis A, Lo K, Menon S, Novakov T, Perlwitz J, Russell G, Schmidt GA, Tausnev N (2005a) Earth's energy imbalance: confirmation and implications. Science 308(5727):1431–1435

Hansen J, Sato M, Ruedy R, Nazarenko L, Lacis A, Schmidt GA, Russell G, Aleinov I, Bauer M, Bauer S, Bell N, Cairns B, Canuto V, Chandler M, Cheng Y, Genio AD, Faluvegi G, Fleming E, Friend A, Hall T, Jackman C, Kelley M, Kiang N, Koch D, Lean J, Lerner J, Lo K, Menon S, Miller R, Minnis P, Novakov T, Oinas V, Perwitz Ja., Perlwitz Ju., Rind D, Romanou A, Shindell D, Stone P, Sun S, Tausnev N, Thresher D, Wielicki B, Wong T, Yao M, Zhang S (2005b) Efficacy of climate forcings. J Geophys Res 110(D18104). DOI: 10.1029/2005JD005776

Haug GH, Hughen KA, Sigman DM, Peterson LC, Röhl U (2001) Southward migration of the intertropical convergence zone through the Holocene. Sicence 293(5533):1304–1308

Haug GH, Günther D, Peterson LC, Sigman DM, Hughen KA, Aeschlimann B (2003) Climate and the collapse of Maya civilization. Science 299(5613):1731–1735

Held IM, Soden BJ (2000) Water vapor feedback and global warming. Annu Rev Energy Environ 25:441–475

Hendy EJ, Gagan MK, Alibert CA, McCulloch MT, Lough JM, Isdale PJ (2002) Abrupt decrease in tropical Pacific sea surface salinity at end of Little Ice Age. Science 295(5559):1511–1514

Hodell DA, Brenner M, Curtis JH, Guilderson T (2001) Solar forcing of drought frequency in the Maya lowlands. Science 292(5520):1367–1370

Hoffmann G (2003) Taking the pulse of the tropical water cycle. Science 301(5634):776–777

Hoffmann G, Ramirez E, Taupin JD, Francou B, Ribstein P, Delmas R, Dürr H, Gallaire R, Simões J, Schotterer U, Stievenard M, Werner M (2003) Coherent isotope history of Andean ice cores over the last century. Geophys Res Lett 30(4):1179. DOI:10.1029/2002GL014870

Hughes MK, Graumlich LJ (1996) Climatic variations and forcing mechanisms of the last 2000 years. Multi-millennial Dendroclimatic Studies from the western United States, vol. 141 of NATO ASI Series, Springer, Berlin Heidelberg New York, pp 109–124

Hughes MK, Xiangding W, Xuemei S, Garfin GM (1994) A preliminary reconstruction of rainfall in north-central China since A.D. 1600 from tree-ring density and width. Q Res 42:88–99

Jones PD, Mann ME (2004) Climate over past millennia. Rev Geophys 42(RG2002). DOI:10.1029/2003RG000143

Jones PD, New M, Parker DE, Martin S, Rigor IG (1999) Surface air temperature and its changes over the past 150 years. Rev Geophys 37(2):173–199

Jones PD, Osborn TJ, Briffa KR (2001) The evolution of climate over the last millennium. Science 292(5517):662–667

Kiehl JT, Gent PR (2004) The community climate system model, version 2. J Climate 17:3666–3682

Knutti R, Stocker TF, Joos F, Plattner GK (2002) Constraints on radiative forcing and future climate change from observations and climate model ensembles. Nature 416(6882):719–723

Knutti R, Meehl GA, Allen MR, Stainforth DA (2006) Constraining climate sensitivity from the seasonal cycle in surface temperature. J Climate (in press)

Lean J, Skumanich A, White O (1992) Estimating the sun's radiative output during the Maunder Minimum. Geophys Res Lett 19(15):1591–1594

Lean J, Beer J, Bradley R (1995) Reconstruction of solar irradiance since 1610: implications for climate change. Geophys Res Lett 22(23):3195–3198

Lindzen RS, Nigam S (1987) On the role of sea surface temperature gradients in forcing low-level winds and convergence in the tropics. J Atmos Sci 44(17):2418–2436

Luterbacher J, Xoplaki E, Dietrich D, Rickli R, Jacobeit J, Beck C, Gyalistras D, Schmutz C, Wanner H (2002) Reconstruction of sea level pressure fields over the eastern North Atlantic and Europe back to 1500. Clim Dyn 18(7):545–561

Luterbacher J, Dietrich D, Xoplaki E, Grosjean M, Wanner H (2004) European seasonal and annual temperature variability, trends, and extremes since 1500. Science 303(5663):1499–1503

Mann ME, Bradley RS, Hughes MK (1999) Northern Hemisphere temperatures during the past millennium: inferences, uncertainties, and limitations. Geophys Res Lett 26(6):759–762

Mann ME, Cane MA, Zebiak SE, Clement A (2005) Volcanic and solar forcing of the tropical Pacific over the past 1000 years. J Climate 18(3):447–456

Mitchell JFB, Karoly DJ, Hegerl GC, Zwiers FW, Allen MR, Marengo J (2001) Detection of climate change and attribution of causes. Houghton JT, Ding Y, Griggs DJ, Noguer M, van der Linden PJ, Dai X, Maskell K, Johnson CA (eds) Climate change 2001: the scientific basis, Chap 12. Cambridge University Press, Cambridge, pp 695–738, contribution of Working Group I to the Third Assessment Report of the Intergovenmental Panel on Climate Change, 881pp

Moberg A, Sonechkin DM, Holmgren K, Datsenko NM, Karlén W, Lauritzen SE (2005) Highly variable Northern Hemisphere temperatures reconstructed from low- and high-resolution proxy data. Nature 433(7026):613–617

Osborn TJ, Briffa KR (2006) The spacial extent of 20th-century warmth in the context of the past 1200 years. Science 311(5762):841–844

Pederson N, Jacoby GC, D'Arrigo RD, Cook ER, Buckley BM, Dugarjav C, Mijiddorj R (2001) Hydrometeorological reconstructions for northeastern Mongolia derived from tree rings: 1651–1995. J Climate 14(5):872–881

Ramaswamy V, Boucher O, Haigh J, Hauglustaine D, Haywood J, Myhre G, Nakajima T, Shi GY, Solomon S (2001) Radiative forcing of climate change. Houghton JT, Ding Y, Griggs DJ, Noguer M, van der Linden PJ, Dai X, Maskell K, Johnson CA (eds) Climate change 2001: the scientific basis, Chap 6. Cambridge University Press, Cambridge, pp 349–416, contribution of Working Group I to the Third Assessment Report of the Intergovenmental Panel on Climate Change, 881pp

Rind D, Overpeck J (1993) Hypothesized causes of decade-to-century-scale climate variability: climate model results. Q Sci Rev 12:357–374

Rind D, Lean J, Healy R (1999) Simulated time-dependent climate response to solar radiative forcing since 1600. J Geophys Res 104(D2):1973–1990

Rind D, Shindell D, Perlwitz J, Lerner J, Lonergan P, Lean J, McLinden C (2004) The relative importance of solar and anthropogenic forcing of climate change between the Maunder Minimum and the present. J Climate 17(5):906–929

Robertson A, Overpeck J, Rind D, Mosley-Thompson E, Zielinski G, Lean J, Koch D, Penner J, Tegen I, Healy R (2001) Hypothesized climate forcing time series for the last 500 years. J Geophys Res 106(D14):14783–14803

Robock A, Liu Y (1994) The volcanic signal in Goddard Institute for Space Studies three-dimensional model simulations. J Climate 7(1):44–55

Robock A, Mao J (1995) The volcanic signal in surface temperature observations. J Climate 8(5, Part 1):1086–1103

Salzer MW, Kipfmueller KF (2005) Reconstructed temperature and precipitation on a millennial timescale from tree-rings in the southern Colorado Plateau, U.S.A. Clim Chan 70(3):465–487

Schmidt GA, Shindell DT, Miller RL, Mann ME, Rind D (2004) General circulation modelling of Holocene climate variability. Q Sci Rev 23(20–22):2167–2181

Shindell DT, Schmidt GA, Mann ME, Rind D, Waple A (2001a) Solar forcing of regional climate change during the Maunder Minimum. Science 294(5549):2149–2152

Shindell DT, Schmidt GA, Miller RL, Rind D (2001b) Northern Hemisphere winter climate response to greenhouse gas, ozone, solar, and volcanic forcing. J Geophys Res 106(D7):7193–7210

Stahle DW, Cleaveland MK (1992) Reconstruction and analysis of spring rainfall over the southeastern U.S. for the past 1000 years. Bull Am Meteor Soc 73(12):1947–1961

von Storch H, Zorita E, Jones JM, Dimitriev Y, González-Rouco F, Tett SFB (2004) Reconstructing past climate from noisy data. Science 306(5696):679–682

Stott PA, Tett SFB (1998) Scale-dependent detection of climate change. J Climate 11(12):3282–3294

Thompson LG, Mosley-Thompson E, Bolzan JF, Koei BR (1985) A 1500-year record of tropical precipitation in ice cores from the Quelccaya ice cap, Peru. Science 229(4717):971–973

Thompson LG, Mosley-Thompson E, Dansgaard W, Grootes PM (1986) The Little Ice Age as recorded in the stratigraphy of the tropical Quelccaya ice cap. Science 234(4774):361–364

Touchan R, Garfin GM, Meko DM, Funkhouser G, Erkan N, Hughes MK, Wallin BS (2003) Preliminary reconstructions of spring precipitation in southwestern Turkey from tree-ring width. Int J Climatol 23(2):157–171

Verschuren D, Laird KR, Cumming BF (2000) Rainfall and drought in equatorial east Africa during the past 1,100 years. Nature 403(6768):410–414

Weaver AJ, Duffy PB, Eby M, Wiebe EC (2000) Evaluation of ocean and climate models using present-day observations and forcing. Atmos Ocean 38:271–301

Wentz FJ, Schabel M (2000) Precise climate monitoring using complementary satellite data sets. Nature 403(6768):414–416

Yoshimori M, Stocker TF, Raible CC, Renold M (2005) Externally forced and internal variability in ensemble climate simulations of the Maunder Minimum. J Climate 18(20):4253–4270

Zorita E, von Storch H, Gonzalez-Rouco FJ, Cubasch U, Luterbacher J, Legutke S, Fischer-Bruns I, Schlese U (2004) Climate evolution in the last five centuries simulated by an atmosphere-ocean model: Global temperatures, the North Atlantic Oscillation and the late Maunder Minimum. Meteorol Zeitschrift 13(4):271–289